OPTICA

Electro-optic sampling of classical and quantum light

Ileana-Cristina Benea-Chelmus,[1,2] Jérôme Faist,[3] Alfred Leitenstorfer,[4] Andrey S. Moskalenko,[5] Ioachim Pupeza,[6,7,8,9] Denis V. Seletskiy,[10] and Konstantin L. Vodopyanov[11,*]

[1]Hybrid Photonics Laboratory, École Polytechnique Fédérale de Lausanne (EPFL), Lausanne CH-1015, Switzerland
[2]Center for Quantum Science and Engineering (EPFL), Lausanne CH-1015, Switzerland
[3]Institut für Quantenelektronik, ETH Zürich, 8093 Zürich, Switzerland
[4]Department of Physics and Center for Applied Photonics, University of Konstanz, D-78457 Konstanz, Germany
[5]Department of Physics, KAIST, 34141 Daejeon, Republic of Korea
[6]Physics Department and State Research Center OPTIMAS, University of Kaiserslautern-Landau, 67663 Kaiserslautern, Germany
[7]Leibniz Institute of Photonic Technology, Albert-Einstein-Straße 9, 07745 Jena, Germany
[8]Cluster of Excellence Balance of the Microverse, Friedrich Schiller University Jena, Jena, Germany
[9]Fraunhofer Institute for Industrial Mathematics ITWM, 67663 Kaiserslautern, Germany
[10]femtoQ lab, Department of Engineering Physics, Polytechnique Montréal, Montréal, Quebec H3T 1J4, Canada
[11]CREOL, College of Optics and Photonics, University of Central Florida, Orlando, Florida 32816, USA
*vodopyanov@creol.ucf.edu

Received 16 October 2024; accepted 15 February 2025; published 17 April 2025

Full characterization of electric-field waveforms in amplitude and phase is achieved across the terahertz to visible spectral range through interaction with an optical pulse shorter than a half-cycle period via the Pockels (linear electro-optic) effect. This technique of electro-optic sampling has become an indispensable tool in various areas, including ultrafast pump-probe, time-domain and frequency-comb spectroscopies, quantum optics, high-harmonic generation, and attosecond science, and holds great promise for further advances. Not only does it enable spectroscopic measurements with record dynamic range and temporal resolution, along with massively parallel real-time spectral data acquisition, but its remarkable sensitivity also allows the detection of vacuum fluctuations, i.e., "zero-point motion" of electric fields, profoundly impacting our understanding of the fundamental laws of nature.

https://doi.org/10.1364/OPTICA.544333

1. INTRODUCTION

The Pockels effect, or linear electro-optic (EO) effect, causes a variation in a material's refractive index, which is proportional to an applied electric field [1]. It occurs in crystals that lack inversion symmetry, such as monopotassium phosphate (KDP), lithium niobate ($LiNbO_3$), beta-barium borate (BBO), barium titanate (BTO), zinc telluride (ZnTe), gallium phosphide (GaP), gallium selenide (GaSe), or organic crystals, such as 4-N, N-dimethylamino-4'-N'-methyl-stilbazolium tosylate (DAST), and other non-centrosymmetric media. The main application of Pockels elements in photonics is their use as voltage-controlled optical retardation waveplates for high-speed amplitude or phase modulators. The most recent applications are in quantum key distribution [2] and in generating electro-optic frequency combs via phase modulation of a narrow-linewidth laser [3].

In 1983, Valdmanis *et al*. pioneered EO sampling (EOS), applying the Pockels effect to characterize ultrafast voltage transients with sub-picosecond rise times by detecting the change in the polarization state imposed by a transient on femtosecond pulses propagating through a lithium tantalate ($LiTaO_3$) EO crystal with a variable delay [4]. Averaging over several minutes, they achieved a voltage sensitivity of 50 μV. The measurements were remarkably immune to electromagnetic noise near the detector. Shortly thereafter, Auston *et al*. used the Pockels effect for coherent detection of terahertz (THz) transients [5]. Waveforms of one cycle duration were generated by optical rectification (the inverse EO effect) of femtosecond pulses in lithium tantalate and probed using optical pulses derived from the same mode-locked laser in the same crystal at a variable time delay. Electro-optic sampling in free space represented the next challenge due to the strong losses that arise when coupling THz signals out of an emitter and back into a detector with a high refractive index [6,7]. Since then, remarkable progress has been made in detecting electric-field waveforms at THz [6–8], mid-infrared (MIR) [9–11], near-IR [12–14], and even visible [15] frequencies. In addition, the powerful technique of time-domain spectroscopy has emerged [16–19]—a formidable method for measuring the optical properties of materials by studying the change in time-domain waveforms of input and propagated

pulses. Subsequent Fourier analysis provides access to frequency-dependent dispersion and absorption (real and imaginary parts of the dielectric function) of a sample. Since it is based on femtosecond pulse trains, the technique has found widespread applications in pump-probe-type experiments on ultrafast dynamical processes. Early examples of such studies are represented in Refs. [20–22]. Today, many time-resolved and non-linear investigations have been performed exploiting EOS.

We note that competing field-resolving techniques, such as TIPTOE (tunneling ionization with a perturbation for the time-domain observation of an electric field), which probes the electric field of a longwave "signal" pulse by observing the modulation of the ionization yield induced by the signal field [24], and ABCD (air-biased coherent detection), which relies on four-wave mixing in air plasma to generate a second harmonic signal carrying information about the measured field [25,26], both require intense laser pulses. Therefore, these methods are incompatible with high repetition rates (50–100 MHz), which are essential for achieving a high signal-to-noise ratio in the measurements.

The structure of this review is as follows. First, we provide the fundamentals of EOS, including the Pockels effect picture, the non-linear wave mixing picture, and the quantum picture. Next, we discuss the applications of EOS in linear spectroscopy, such as wide dynamic range spectroscopy of biological systems and high-resolution molecular spectroscopy in the gas phase, with massive spectral data acquisition in real time. We move on to quantum research, which involves probing the quantum vacuum directly in the time domain and through correlation measurements. Finally, we discuss cutting-edge concepts such as strong-conversion EOS, quantum state tomography, back action, quantum probes, and relativistic aspects of EOS, while also outlining future research directions.

2. ELECTRO-OPTIC DETECTION

A. Pockels Effect Picture

Perhaps the most accessible understanding of EOS is obtained by considering its most common geometry, employing a zincblende-type EO crystal (EOX) with simple (cubic) symmetry and no birefringence, such as ZnTe, GaAs, or GaP. This sensor is oriented in such a way that the beam propagates along the $[1\bar{1}0]$ direction of the crystal, and the directions [110] and [001] are in the plane perpendicular to the beam [Fig. 1(a)]. The input beam contains a test wave (the wave to be measured) that is linearly polarized along the [110] direction, and a gate pulse that samples the test wave is linearly polarized along the [001] direction. The gate pulse is commonly centered at frequencies higher than that of the test wave and has a pulse duration that is shorter or comparable to half an oscillation cycle of the test wave.

The electric field of the test wave (E_T) transiently induces birefringence in the EOX along directions at $\pm 45^\circ$ relative to the [001] direction in the plane normal to the beam [X′, Y′ in Fig. 1(a)]. The induced birefringence is monitored by the gate pulse. The change in the refractive index along X′ and Y′ is $\pm\Delta n$ and varies proportionally to the field strength of the test wave: $\Delta n = \frac{1}{2} r_{41} n^3 E_T$. Here, r_{41} is the corresponding electro-optic tensor element, and n is the linear refractive index of the EOX at the frequency of the gate pulse. The polarization components of the gate pulse along X′ and Y′ acquire opposite phase shifts $\pm\Gamma$ given by $\Gamma = \frac{\omega l}{c}\Delta n$, with l denoting the EOX thickness, ω the central angular frequency of the gate pulse, and c the speed of light.

As illustrated in Fig. 1 (a), the gate pulse, which is linearly polarized in the absence of E_T ($\Gamma = 0$), becomes slightly elliptically polarized after the EOX, with clockwise or counter-clockwise polarization rotation depending on the sign of E_T. Adding a $\lambda/4$ plate adds a $\pi/2$ phase shift along the axis Y′, so that the polarization of the gate pulse is modified in such a way that it is circularly

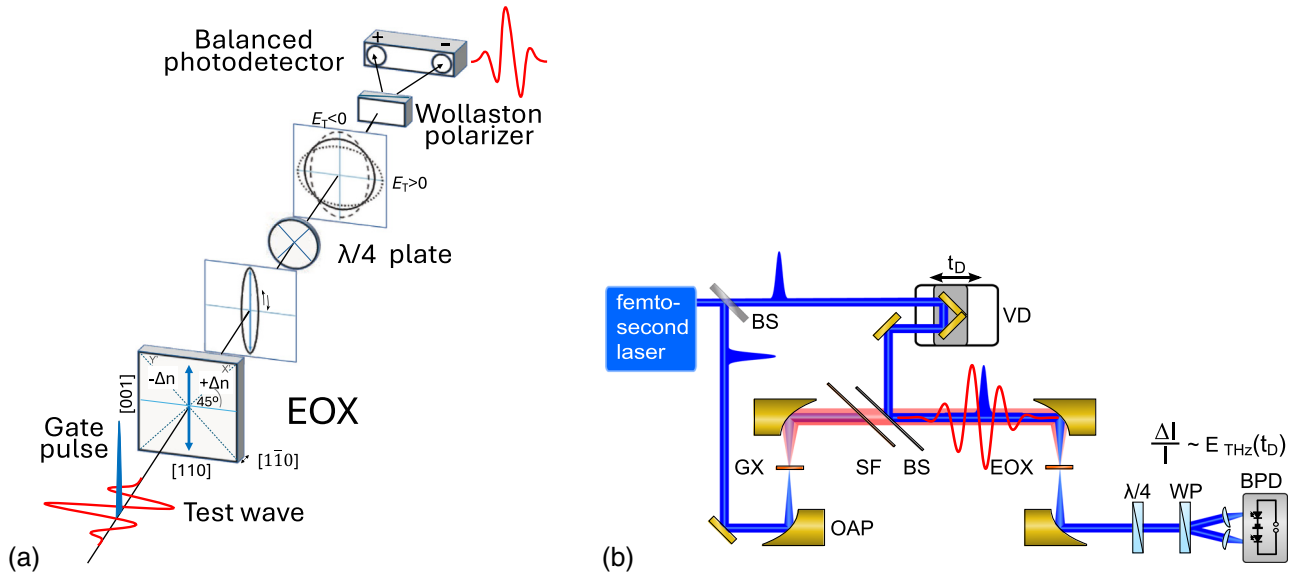

Fig. 1. (a) Geometry of the incoming fields, electro-optic crystal (EOX), and the evolution of the polarization state of the gate pulse. (b) A typical setup for EOS with a femtosecond laser. The near-infrared (NIR) laser output in the form of short pulses (blue) is split by a beam splitter (BS) into the "test" and "gate" beams. The longwave test waves (red), produced, e.g., by optical rectification of the laser output, are combined with the gate pulses (the laser output pulses) and are analyzed via ellipsometry. OAP: off-axis parabolic mirror; GX: crystal for generating test waves; SF: long-pass spectral filter; BS: beam splitter/combiner; VD: variable optical delay line; EOX: electro-optic crystal; $\lambda/4$: quarter-wave plate; WP: Wollaston polarizer; BPD: balanced pair of photodiodes. (b) is adapted from Ref. [23].

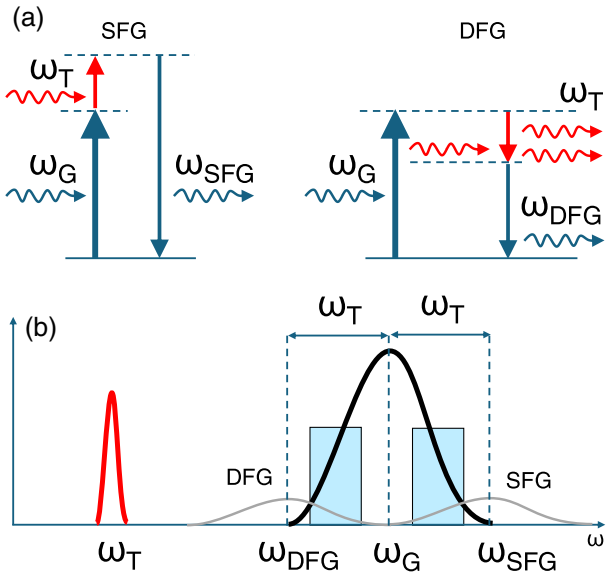

Fig. 2. Three-wave mixing picture of EOS. (a) The SFG and DFG processes. (b) Spectra of the test waveform (red), gate pulse (black), and SFG/DFG waveforms (gray). The rectangles in light blue indicate the optimal spectral filtering for DFG and SFG processes.

polarized at $\Gamma = 0$ and acquires elongation in the vertical or horizontal direction at $\Gamma \neq 0$, depending on the sign of E_T [Fig. 1(a)]. Subsequent analysis uses a Wollaston polarizer that separates the vertical and horizontal polarization components and a balanced photodetector. One can show (see [23]) that the relative differential current of the balanced photodetector is

$$\frac{\Delta I}{I} = \frac{I_{vert} - I_{hor}}{I_{vert} + I_{hor}} = \sin 2\Gamma \approx 2\Gamma = \frac{\omega l}{c}\Delta n = \frac{\omega l r_{14} n^3}{c} E_T, \quad (1)$$

where I_{vert} and I_{hor} are the detector currents induced by the vertical and horizontal polarization components of the gate, respectively. This approximation holds in the limit of small non-linear phase shifts $\Gamma \ll 1$ and under the condition that the gate pulse is considerably shorter than the characteristic time scale of the test wave, given by its oscillation cycle. In this case, a linear dependence of $\frac{\Delta I}{I}$ on the test wave field E_T results. By varying the time delay t_D between the test wave and the gate, the entire waveform $E_T(t)$ is sampled. A typical setup for EOS with a femtosecond laser is depicted in Fig. 1(b).

B. Three-Wave Mixing Picture

While the Pockels effect picture provides a good operational understanding of the principle of EOS, it effectively relies on a time-independent treatment of the test wave field E_T. In this scenario, the picture corresponds to the limit where the field's center frequency ω_T vanishes, thereby obscuring a quantitative description of EOS from both an electrodynamic and quantum perspective. To address this, we consider a non-linear optical polarization arising from the interaction between the gate field E_G at the center angular frequency ω_G and E_T, a description of EOS first given by Gallot and Grischkowsky [8]. The treatment up to the terms proportional to the second-order non-linear-optical susceptibility tensor $\chi^{(2)}$ gives rise to the sum- and difference-frequency generation (SFG and DFG) processes when all three fields co-propagate through the EOX. The EOX is typically configured in such a way that the spectral sidebands of the gate, induced by ω_T, $\omega_{SFG} = \omega_G + \omega_T$, and $\omega_{DFG} = \omega_G - \omega_T$ are orthogonally polarized with respect to E_G field ($E_G \perp E_{SFG}, E_{DFG}$). A combination of a wave plate and a polarizer is used to project these wave-mixing products onto the gate's field, giving rise to a phase modulation Γ (being proportional to E_T), which can be read out via ellipsometry, as presented in the previous section. It follows that (i) the interaction between the waves must be phase-matched, (ii) the EOX must be thin enough to avoid time-domain walk-off due to the group velocity mismatch between waveforms with different center frequencies, and (iii) the spectrum must be wide enough, $\Delta\omega_G > \omega_T$, so that its sidebands overlap with the spectrum of the gate pulse. Formally, condition (iii) is equivalent to the above-mentioned "subcycle" requirement that the gate pulse duration (τ_G) has to be shorter than the characteristic time scale of the test wave since for pulses close to the bandwidth limit $\tau_G \sim 1/\Delta\omega_G$ holds.

The subcycle requirement also represents a case that can be referred to as a "sideband-unresolved." The sidebands cannot be distinguished in the region of the spectral overlap between co-polarized SFG/DFG and the gate, thus allowing for the measurement of the field *amplitude* of E_T through the interferometric phase Γ. This is a special case with respect to a more common "sideband resolved" scenario of three-wave mixing, where $\Delta\omega_G \ll \omega_T$ holds and interference is lost due to a vanishing spectral overlap between the sidebands and the gate in between. In this regime, the SFG and DFG processes can be viewed as energy up- and down-conversion interactions (with respect to the gate's photon energy), respectively. Formally, an annihilation of a gate photon at a frequency ω_G (and a test photon at ω_T) leads to the creation of an upconverted sideband photon at ω_{SFG} (a downconverted sideband photon at ω_{DFG} and a photon at ω_T) in the SFG (DFG) process. The scenario is illustrated in Fig. 2(a), where vertical up (down) arrows represent photon annihilation (creation) processes. These processes can be visualized to represent an energy (particle) flow from ω_G and ω_T to the ω_{SFG} and ω_{DFG} sidebands.

How does this description recover the Pockels picture, where the gate and the test waves interact through a phase shift, proceeding without energy exchange between the two? First, note that the number of test-wave photons remains unchanged if both sidebands are considered jointly. Indeed, a loss of a test-wave photon in the SFG process is compensated by the creation of a test-wave photon through the DFG process. This way, we can ensure that the test wave remains unperturbed in the wave mixing. How about ω_G? In the sideband resolved regime, energy flows from ω_G into the ω_{SFG} and ω_{SFG} products. Hence, our second requirement is to treat ω_G, ω_{SFG}, and ω_{DFG} jointly. Indeed, by imposing the subcycle condition ($\Delta\omega_G > \omega_{SFG} - \omega_{DFG}$), the resulting spectral overlaps ensure no energy loss from (and constancy of) the formed composite wave. Therefore, operation in the subcycle regime with symmetric treatment of the entire gate spectrum restores the Pockels picture, leaving both the test and gate waves unperturbed (up to the second order). The phase of the interaction is revealed through interference of the gate pulse with the spectral products produced by the superposition of the energy up- and down-conversion processes (SFG and DFG).

The symmetric treatment of the gate spectrum requires phase matching of both the SFG and DFG processes, which is typically achieved in relatively thin non-linear crystals, particularly when the frequencies of E_T lie in the MIR [12,27]

or higher. In the low-frequency regime (e.g., THz), the wavevector-matching condition $k_G \pm k_T - k_{SFG/DFG} = 0$ can be simplified [7] toward a picture of matching the phase velocity of the test wave v_T with the group velocity of the gate pulse, $v_G^g \equiv d\omega/dk|_{k=k_G} \approx \omega_T/|k_G - k_{SFG/DFG}| = \omega_T/k_T$. This typically allows for the use of thicker EO crystals while preserving the sideband symmetry in the detection. For even higher frequencies (e.g., near-infrared) and/or thicker crystals, efficient phase matching can be typically supported for only one of the sidebands (see Section 3.C.3 for an exception to this rule). A filter that selects a band of maximal spectral overlap between the phase-matched process and the gate wave [28–30] [Fig. 2(b)] can allow for an optimization of the measurement's signal-to-noise ratio and hence the detection dynamic range (see also Section 3). Such an asymmetric detection strategy requires careful calibration due to the uncompensated photon flow between the gate and the test waves. The symmetric treatment of the sidebands has a dramatic consequence on the quantum analysis of the test wave, elaborated in Section 4.

For symmetric detection, $E_{DFG+SFG} \equiv E_{DFG} + E_{SFG}$, the photon-number difference signal from the photodiodes $S_{eo} = N_1 - N_2$ can be represented as [8,16,31,32]

$$S_{eo} = C \int_0^\infty d\omega \frac{1}{\hbar\omega} \left[E_G^*(\omega) E_{DFG+SFG}(\omega) + \text{c.c.} \right]. \quad (2)$$

Here, $C = 4\pi c n \epsilon_0 A$, with ϵ_0 being the vacuum permittivity, $\hbar$ the reduced Plank constant and A the effective transverse area determined by the beam waist of E_G at the EOX, which should be adjusted optimally with respect to the transverse extension of E_T. The symbol * denotes complex conjugation, and c.c. represents the complex conjugated counterpart of the first term in the brackets. Evaluation of Eq. (2) in order to express it via E_T leads to

$$S_{eo} \equiv S_{eo}(t_D) = C' \int_{-\infty}^{\infty} d\Omega E_T(\Omega) R(\Omega) e^{-i\Omega t_D}, \quad (3)$$

where $C' \approx -n^3 r_{41} l N \omega_G / c$, with N being the total number of photons in the gate pulse. $R(\Omega)$ is the gating function, depending on the frequency Ω of the test wave from the frequency interval centered at ω_T. It is determined by both the gate pulse properties and phase-matching conditions. For an idealized delta-function–like gate pulse and perfect phase matching, $R(\Omega) = 1$, Eq. (3) reduces to $S_{eo}(t_D) \sim E_T(t_D)$, thus recovering the expected result from the Pockels picture. In case the complex response function due to finite phase mismatch is known, correction of a transient may be straightforwardly performed in the frequency domain [10]. Accounting for the finite gating pulse duration τ_G, we get $S_{eo}(t_D) \sim \int_{-\infty}^{\infty} dt E_T(t) R(t - t_D)$, with the gating function in the time domain $R(t)$ being given by the envelope of the gating pulse. If $R(t)$ is not short enough, a sufficiently precise recovery of $E_T(t_D)$ based on the measured signal $S_{eo}(t_D)$ is still possible by determining and then deconvolving of $R(t)$ from the signal $S_{eo}(t_D)$ [33], though potentially causing a reduction in the signal-to-noise ratio.

C. Quantum Picture

As we saw in the previous section, EOS can directly access a time-dependent field amplitude. Nevertheless, the previous discussion has focused on classical electric fields, while quantum aspects such as vacuum noise, photonic correlations, or entanglement were neglected. In the following section, we extend the description of EOS to the quantum regime. Homodyne detection (HD) represents an established approach to the quantum properties of electromagnetic fields [34]. Here, the input quantum field $\hat{E}_Q$ is mixed with a strong classical beam, typically termed the local oscillator E_{LO}, on a linear beam splitter (BS) [Fig. 3(a)]. For a sufficiently strong LO, the total noise of such a measurement is not sensitive to the vacuum fluctuations of the LO beam and instead is dominated by quantum statistics of $\hat{E}_Q$. HD is intrinsically a frequency-domain technique, as it evaluates the field $\hat{E}_Q$ at a frequency position of the E_{LO} [Fig. 3(b)]. As we see in this section, EOS can also be viewed as a special (non-linear) case of homodyne detection which, however, gives access to the field $\hat{E}_Q$ localized in time.

To provide a quantum picture of the EOS, we need to replace E_T in Eq. (3), and before (implicitly), in the expression for $E_{DFG+SFG}$ in Eq. (2), by the corresponding operator $\hat{E}_T$ [32]. Moreover, for the gate pulse field, apart from its classical coherent amplitude, we have to also consider a contribution stemming from the vacuum fluctuations in its corresponding frequency range. As a result, the signal produced by the ellipsometry setup can be interpreted in terms of homodyne detection [Fig. 3(a)]. The primary difference with the frequency-domain homodyne detection arises from the non-linear mixing process involved in the EOS. Indeed, as shown in Section 2.B, the detection takes place in the frequency range of the gate pulse, with the test wave upconverted to that range via the three-wave mixing process. Thus, the EOS can be seen as a time-domain homodyne detection of the quantum field $\hat{E}_Q$, entering one of the ports of the beam splitter (BS) and resulting from the preceding upconversion of $\hat{E}_T$ by the gate pulse, which simultaneously plays a role of the local oscillator injected at the other port. It is important to keep in mind that the two incoming ports of the beam splitter in the HD correspond to the two polarization directions of the field entering the Wollaston prism in the case of the EOS. As usual for the homodyne detection, we can neglect vacuum correction at the input port with the strong coherent LO (but not the other port!) in Fig. 3(a), so we effectively have $E_{LO} \equiv E_G$.

The input quantum field consists of two parts. The signal part $\hat{E}_Q$ is given by $\hat{E}_{DFG+SFG} \sim E_{LO}\hat{E}_T$ in the time domain [cf. Fig. 3(e)] and contains information on the test wave field $\hat{E}_T$. The noise part is given by $\delta\hat{E}_{LO}$ [green in Fig. 3(a)], corresponding to the vacuum fluctuations. $\hat{E}_{DFG+SFG}$ ($\delta\hat{E}_{LO}$) leads to the contribution $\hat{S}_Q \equiv \hat{S}_{eo} \sim I_{LO}\hat{E}_T$ ($\hat{S}_{sn} \sim E_{LO}\delta\hat{E}_{LO}$) in the total signal operator $\hat{S} = \hat{S}_Q + \hat{S}_{sn}$. Naturally, the $\delta\hat{E}_{LO}$ is not connected to any signal we want to measure. Such a term is absent for the frequency-domain HD, provided the LO is sufficiently strong. Thus, the shot noise of the LO is intrinsic to the quantum EOS measurements and needs to be appropriately considered in the analysis of quantum signals (Section 4). It is important to note that the contamination of the EOS signal by the shot-noise contribution $\hat{S}_{sn}$ does not affect the analysis of the classical fields as this contribution can be made sufficiently small upon averaging an appropriate number of independent measurements.

It is insightful to familiarize the time-domain aspect of the EOS by contrasting it with the frequency-domain homodyne detection in more detail. In the conventional scheme, a (generally quantum) field under study [labeled $\hat{E}_Q \equiv \hat{E}_T$ (red) in Fig. 3(b), centered

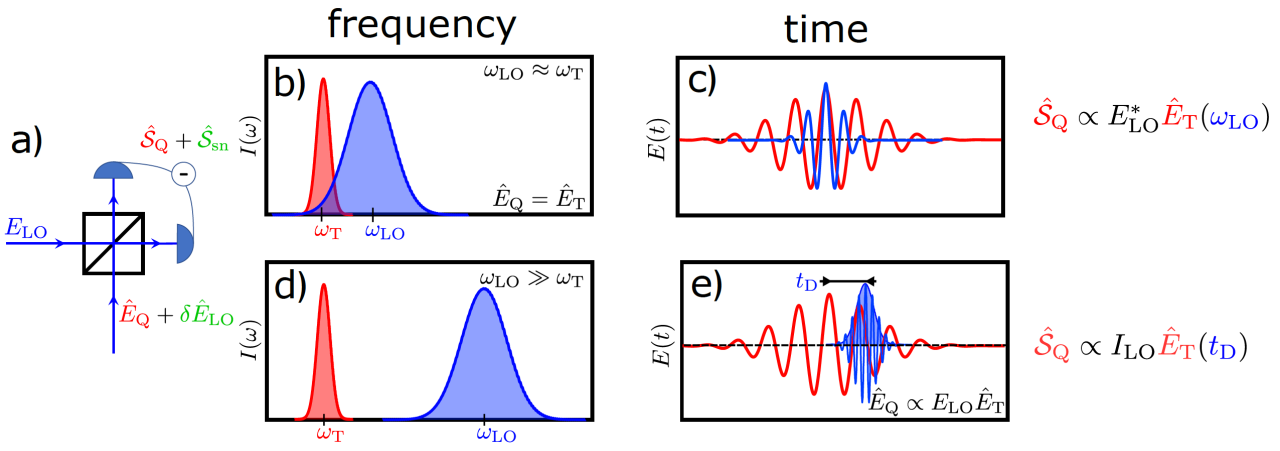

Fig. 3. (a) Schematic of a non-linear homodyne detection, where the EOS is interpreted as a "frequency upconversion" followed by the regular homodyne detection. Two incoming signals are mixed at a 50/50 beam splitter (BS) and the difference signal is then read out from a pair of balanced photon detectors. There is no term equivalent $\delta\hat{E}_{LO}$ at the signal input port of the BS for frequency-domain homodyne detection (HD). (b)–(e) Schematic illustration of the difference between the HD (top row) and EOS (bottom row) in both frequency (left column) and time (middle column) domains and resulting signals $\hat{S}_Q$ acquired in those measurements.

at a frequency ω_T] is directly mixed by means of a 50/50 linear BS with a local oscillator (LO) field E_{LO}, centered at ω_T (blue). The photodetector of frequency detection bandwidth (f_{BW}) can only register the interference beat of the two fields if the spectral detuning $\Delta\omega = |\omega_T - \omega_{LO}|$ between these signals is less than f_{BW}. Even for the fastest detectors available presently, this fact implies that the spectral position (e.g., center frequency ω_{LO}) and the extent of the LO field must, at least partially, overlap with the spectral content of the signal under study, i.e., $\omega_{LO} \approx \omega_T$, as shown in Fig. 3(b). The interference signal $\hat{S}_Q$ provides information on $\hat{E}_T$, localized over the frequency range where $\hat{E}_T \cap E_{LO}$. In other words, $\hat{S}_Q(\omega_{LO}) \propto E^*_{LO}\hat{E}_T(\omega_{LO})$ (top right formula in Fig. 3) underscores the frequency-domain character of the technique, which naturally averages quantum information of the test wave over its multiple optical cycles [Fig. 3(c)]. Due to the necessity of direct detection, such schemes are challenged in the MIR and THz spectral bands by a (in some cases) severe lack of high-efficiency photodetectors, notwithstanding promising recent advances [35].

Now let us re-visit the EOS scheme in the frequency domain [Fig. 3(d)], where we consider a low-frequency input centered at ω_T (e.g., THz or MIR, shown in red), while the short gate pulse, acting as an LO (blue), is represented by a high-frequency signal centered at ω_{LO}, e.g., at near-IR or visible frequency. Direct detection of the beat signal between the two waves is not possible since $\Delta\omega \gg 2\pi f_{BW}$ is on the order of the optical frequency. Indeed, the beat can be obtained only through the frequency upconversion action of the three-wave mixing process (producing SFG/DFG signals, described in Section 2.B) and subsequent interference with the LO field. This process is more directly visualized in the time domain, where $\hat{S}_Q(\tau_D) \propto I_{LO}\hat{E}_T(\tau_D)$ (bottom right formula in Fig. 3). Hence, the test field is directly evaluated at a temporal position τ_D, and the signal's proportionality to the intensity envelope of the LO pulse marks the non-linear optical character of the detection process. Since $\omega_{LO} \gg \omega_T$, it is possible to generate an LO pulse with a duration shorter than the half-cycle of the field $\hat{E}_T$, as depicted in Fig. 3(e), hence providing subcycle information about the test wave. Notice that Fig. 3(e) might remind the time gating by a reference pulse used in the cross-correlation frequency-resolved optical gating (XFROG) technique [36]. However, XFROG is based on the intensity spectrum of the gated test wave $\hat{E}_T(t)$, and its signal is not linear but quadratic in it, which might be disadvantageous for weak $\hat{E}_T(t)$. Moreover, the reconstruction algorithm required to extract $\hat{E}_T(t)$ from the signal acquired by XFROG does not seem to be generally applicable for quantum fields. In contrast, Section 4 shows the applicability of EOS even for the measurement of quantum fields in their ground state, where XFROG would fail.

We can see that both HD and EOS provide localized information about the test field $\hat{E}_T$. In the frequency domain, this is evident by the evaluation of $\hat{E}_T$, prepared at the spectral position ω_{LO}, as in $\hat{S}_Q(\omega_{LO}) \propto E^*_{LO}\hat{E}_T(\omega_{LO})$. In the time domain, the temporal overlap with the LO provides information on $\hat{E}_T$, now localized around a temporal position t_D selected by the LO, as in $\hat{S}_Q(t_D) \propto I_{LO}\hat{E}_T(t_D)$. As such, the parameters of choice of the local oscillator, namely ω_{LO} and t_D, control the signal in the frequency and time domains, respectively.

Contrasting EOS with the frequency-domain HD clarified the important distinctions in the scope of the two approaches. Moreover, it also becomes clear how EOS is different from a traditional parametric down-conversion (PDC) process, used, for example, for the preparation of quantum-correlated photon pairs [37]. Whereas full information about the test field can be obtained when mixing an upconverted signal with the LO, this is generally not possible in the PDC process, where the absence of spectral overlap results in the complete loss of the phase information.

3. EOS IN LINEAR SPECTROSCOPY

After introducing the fundamentals of EOS from an intuitive picture via a rigorous description in the classical regime all the way to the quantum world, we will now address specific applications. For the sake of brevity and with regard to recent progress in the field, we first focus on linear spectroscopy. Of course, owing to its time-resolved character, EOS is also fully compatible with dynamical and non-linear measurements.

A. Precision and Dynamic Range of EOS in the Molecular Fingerprint Region

Among quantitative multivariate molecular analysis techniques, broadband IR vibrational spectroscopy [38,39] uniquely combines several advantages. It requires minimal sample preparation, and the sample-specific "vibrational fingerprint" signal is acquired via optical interrogation, non-destructively and label-free. In addition, interrogating fundamental molecular vibrations in the IR molecular fingerprint region profits from large absorption cross-sections, potentially providing access to a broad range of molecular concentrations. A few prominent examples include the application of Fourier-transform IR (FTIR) spectroscopy as the gold standard for condensed-phase biological samples [40] to investigate and confirm the existence of person-specific IR fingerprints of blood serum and plasma [41], fast hyperspectral imaging of tissue [42], or gas-phase dual-frequency-comb spectroscopy [43,44].

Recent progress in ultrafast laser sources generating waveform-stable pulses with Watt-level average power and broad spectral coverage in the MIR molecular fingerprint region [45–52] opens up new vistas for fast, label-free IR vibrational spectroscopy. Thereby, EOS-based detection has afforded access to a new regime of sensitivity, dynamic range, and acquisition speed surpassing long-standing limitations of direct detection in this spectral region. The use of Watt-level gate pulses along with relatively thick (~0.5 mm) EOX in phase-matched EOS configuration enables multi-percent-level upconversion efficiencies, e.g., via SFG, to the near-IR spectral range. Along with the availability of high-quantum-efficiency detectors at room temperature in this spectral range, this ensures detection at the shot-noise limit. Furthermore, filtering the intense LO allows to operate balanced detectors with an increased dynamic range, which is necessary in broadband detection in the molecular fingerprint region [Fig. 4(a)].

On the other hand, sensitive EOS has been employed as a broadband—both in the radio- and in the optical-frequency domains—diagnostic tool for the stability of IR waveforms [53]. Remarkably, these high-precision measurements have confirmed the exquisite passive phase stability of waveforms obtained via intrapulse DFG (e.g., optical rectification), with jitter values on the order of a few attoseconds, corresponding to sub-mrad phase stability [Fig. 4(b)]. These values are similar to those of state-of-the art linear interferometric measurements [54], despite the added complexity of employing ultrashort pulses and non-linear optics.

B. IR Field-Resolved Spectroscopy of Biological Systems

The combination of the waveform stability of modern ultrafast IR sources with the improvement in sensitivity and detection dynamic range renders EOS-based vibrational spectroscopy highly attractive for applications to biological samples. Importantly, for linear vibrational spectroscopy, precise knowledge of the (linear) EOS instrument response function is not necessary, as the pure sample response can be isolated by frequency-domain referencing, in analogy to conventional, time-integrating spectroscopy [29].

The temporal structure of the response of molecular samples to an impulsive excitation, along with the field-proportionality of the recorded signal, however, bring about several qualitative advantages that justify the nomenclature field-resolved spectroscopy (FRS) even without precise knowledge of the instrument response function. The temporal separation of the resonant sample response

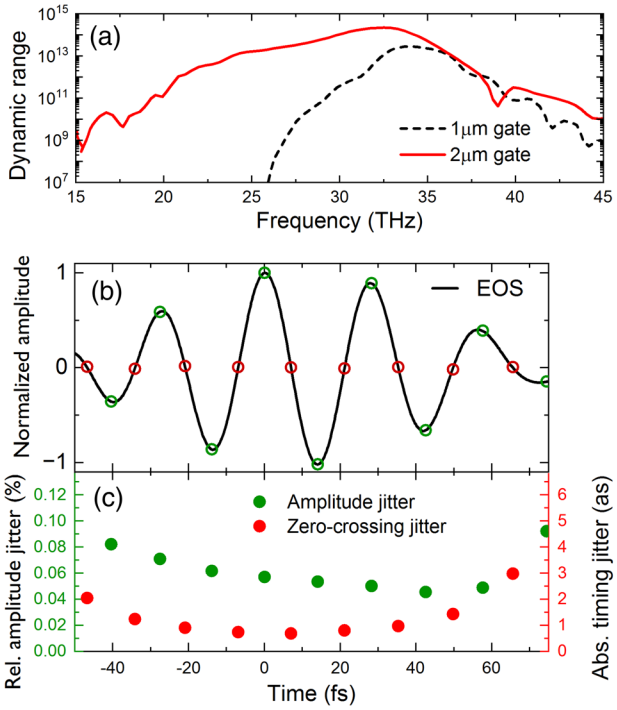

Fig. 4. (a) Intensity dynamic range for state-of-the-art SFG-phase-matched EOS with 1 μm gate pulses (black, dashed line) and 2 μm gate pulses [53] (red, continuous line), both for a scan range of 2.2 ps and 16 s integration time. In both cases, the EOX was GaSe with a thickness of ~0.5 mm. Due to their longer wavelength, gating with 2 μm pulses allowed both for a higher average power (1.8 W) and better phase matching of SFG, resulting in both a higher dynamic range and broader spectral coverage. (b),(c) Measurement of waveform jitter for a few-cycle IR pulse generated via intrapulse DFG. (b) Measured EOS trace. Circles: waveform extrema (green) and zero crossings (red) for measurements in (c). (c) Measured relative amplitude (green) and absolute zero-crossing (red) jitter (standard deviation) across the waveform for the 10 kHz to 0.625 MHz band. The values were obtained by recording EOS signals for fixed delays between the test wave and gate pulse, indicated in the panel (b) by the empty circles. (a) is adapted from Ref. [29]; (b) and (c) are reproduced from Ref. [52].

following the ultrafast excitation [Fig. 5(a), left panel] enables recording the sample-specific spectroscopic information largely without the influence of the excitation that carries the technical noise of the source. This improves the "visibility" of the—often orders of magnitude weaker—molecular signals [29]. With proper referencing, this improvement in the signal-to-noise ratio can be translated to standardized, that is, instrument-independent, spectroscopic fingerprints without loss of sensitivity [55]. These molecular fingerprints carry full amplitude and phase information, reflecting the electric-field-sensitive nature of the measurement. The same temporal separation enables relating the coherent re-emission energy following a few-cycle excitation field to the energy of the latter. This ratio, dubbed spectroscopic efficiency [56], can serve as a guide for designing the measurement conditions for a specific application. Furthermore, the signal measured in FRS scales proportionally to the electric field of the test wave rather than its intensity. This improves the conditions for transmission measurements through strongly-attenuating samples in two ways [57]. First, considering water—ubiquitous in (condensed) biological samples—as a high-absorption matrix, the optimum sample thickness with respect to the detection sensitivity of analytes in

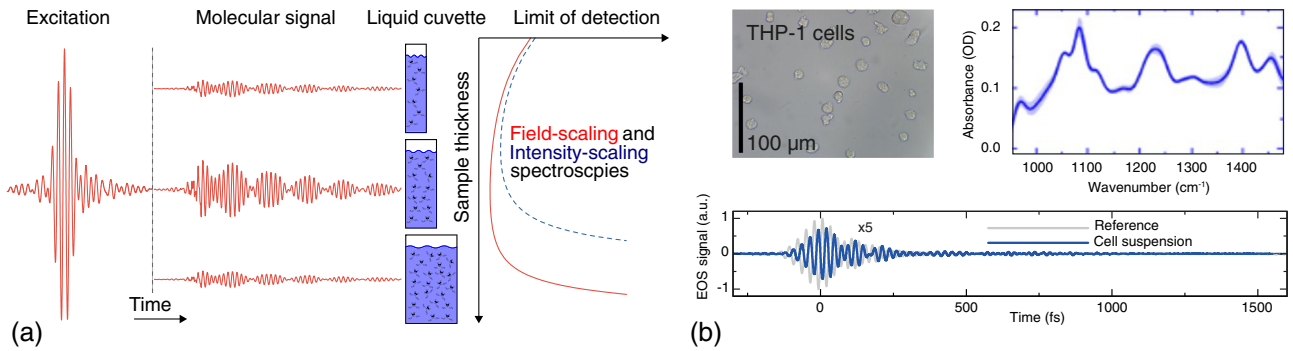

Fig. 5. (a) (adapted from Ref. [57]) Left panel: FRS transmission measurement of an analyte solved in water, illustrated for three sample cuvette thickness values. The resonant response of the $DMSO_2$ molecules follows the few-cycle excitation due to causality. The signal strength of the resonant molecular response relative to the excitation strength exemplifies the scaling of the limit of detection with the sample cuvette thickness, while the case in the middle illustrates the sample thickness for optimum sensitivity, both the thinner and the thicker sample result in a weaker resonant response, due to less analyte molecules in the beam path and due to more attenuating water molecules, respectively. Right panel: illustration of the scaling laws for the limit of detection of an analyte solved in water for field-scaling spectroscopies such as FRS, and for intensity-scaling ones such as FTIR spectroscopy. (b) (adapted from Ref. [29]) FRS transmission measurement through a 0.1 mm thick cuvette containing a suspension of leukemia monocytic cells.

the molecular fingerprint region is ~35 µm, as opposed to significantly shorter distances for intensity-proportional schemes such as FTIR spectroscopy. Second, the limit of detection increases considerably slower for deviations from this optimum sample thickness in field-proportional measurements, in particular toward increasing sample thicknesses [57] [Fig. 5(a), right panel]. This opened the door to high-signal-to-noise broadband IR transmission measurements of biological systems such as cells and plant leaves in their natural, aqueous state for the first time [29] [Fig. 5(b)].

Sampling the oscillating electric field (rather than its cycle-averaged intensity) results in an unprecedented linear-response intensity dynamic range, that is, the ratio of maximum optical power spectral density to the detection noise floor, of $>10^{14}$ [29,58], vastly exceeding that of traditional infrared spectroscopy. Finally, rapid-scan [59–61] or single-shot techniques [62] can overcome slow drifts that otherwise deteriorate the signal-to-noise ratio and, thereby, facilitate operation at the shot-noise limit.

This opens up new possibilities, such as high-throughput fingerprinting of particles in flow, including biological cells or microplastics [63], or rapid sub-wavelength field-resolved microscopy [64–67], which has recently been extended to the entire IR range [68].

C. High-Resolution MIR to THz Molecular Spectroscopy with EOS

1. Dual-Comb Spectroscopy

Dual-comb spectroscopy (DCS) is an advanced version of Fourier transform spectroscopy that utilizes the high temporal coherence of optical frequency combs to enable simultaneous broadband, fast, and high-resolution spectral measurements without moving parts [69–71]. Here, a frequency comb with the repetition rate f_{rep} interrogates the sample and interferes on a fast photodetector with a second comb having a slightly different repetition rate $f_{rep} + \Delta f_{rep}$, such that $\Delta f_{rep}/f_{rep} \approx 10^{-4}-10^{-6}$. In the time domain, the pulses from one comb pass through the pulses of the second comb with a gradually increasing time delay. The interference signal, repeating with a period of $1/\Delta f_{rep}$, is recorded over time and then Fourier-transformed to extract the sample's spectrum. Over the past two decades, DCS has seen rapid advancements, particularly in the MIR and THz spectral regions, which are especially valuable for molecular spectroscopy and trace molecular detection [43,44,72–76].

2. DCS–EOS Measurements

Detecting interferograms in the MIR-THz range using photon detectors remains a significant challenge due to inherently higher noise levels compared to their near-infrared (NIR) counterparts, even under cryogenic conditions. Cowligy *et al*. [77] presented an innovative approach to MIR DCS using EOS for detection, thereby bypassing the need for long-wavelength infrared (LWIR) photodetectors. Here, EOS enables the direct characterization of the field of the LWIR comb that interrogates the sample, providing complete information about the real and imaginary components of the sample's response. The authors used a dual-comb system based on near-IR fibers, with the first comb converted to broadband LWIR for spectroscopic probing of molecular species and the second comb providing EOS gate pulses [77].

Using a new class of ultrafast lasers, Konnov *et al*. performed high-resolution DCS–EOS measurements across a remarkably broad frequency range of 1.5–45 THz (6.6–200 µm) with simultaneously resolving of up to 200,000 spectral data points (comb lines) in real time [78]. As a driving source, the authors used a pair of phase-locked Cr:ZnS ($\lambda = 2.35$ µm) laser combs with a comb-line spacing of 80 MHz [79]. One of the Cr:ZnS combs (Fig. 6) was frequency downconverted via optical rectification (also referred to as intrapulse difference frequency generation, IDFG) in ZGP or GaSe non-linear crystals [49] to produce ultrabroadband long-wavelength combs for probing the sample, while the second comb was frequency doubled and used for EOS gating.

EOS–DCS measurements in the MIR spectral range of $600-1200\ cm^{-1}$ (8–16 µm) with low-pressure gaseous methanol, ethanol, isoprene, and dimethyl sulfide—important biosignature gases for exoplanet exploration—revealed Doppler-limited spectroscopic features of these molecules with unprecedented resolution [78]. The spectral resolution below 10 MHz, which is narrower than the comb-line spacing of 80 MHz, was achieved by interleaving spectra obtained with incrementally shifted frequency

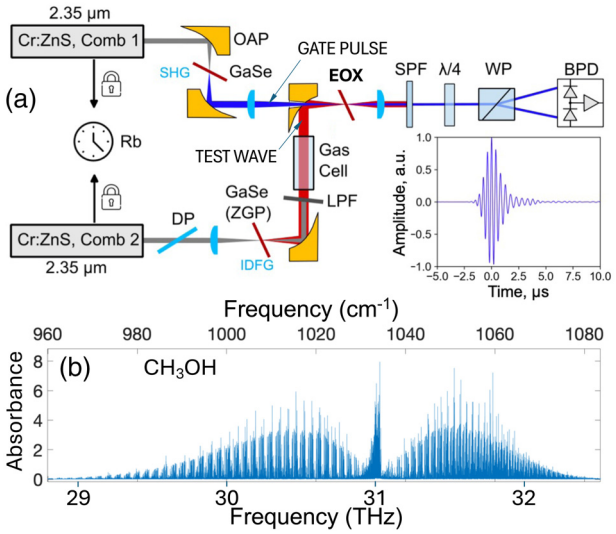

Fig. 6. (a) Schematic of the EOS–DCS spectroscopy setup. DP: dispersive plate for pulse pre-chirping; OAP: off-axis parabolic mirror; LPF: long-pass filter; SPF: short-pass filter; λ/4: quarter-wave plate; WP: Wollaston prism; BPD: InGaAs balanced photodetector. The inset shows the central portion of a typical EOS signal. (b) High-resolution (Doppler-limited) spectrum of the methanol molecule at 0.8 mbar pressure.

combs. A high-resolution spectrum of the methanol (CH_3OH) molecule is presented in Fig. 6(b).

By utilizing optical multipass cells with a 76 m path length or higher [44] or resonant enhancement cavities with effective interaction lengths up to 81 m [80], DCS–EOS in the LWIR range can achieve gas-phase molecular detection sensitivities down to the part-per-trillion level.

3. EOS with Simultaneous SFG and DFG Detection

One of the remarkable capabilities of DCS–EOS is its ability to simultaneously measure both the vibrational bands in the MIR range and the rotational bands in the THz range of the same molecule. In this type of experiment, a carrier-envelope-phase (CEP) stable comb, consisting of two distinct yet mutually coherent wideband spectral regions—a MIR band (10–33 THz, 9–30 μm) and a THz band (2.5–4.5 THz, 67–120 μm)—was generated via IDFG in a GaSe crystal [Fig. 7(a)] [81]. For EOS detection, the authors employed another GaSe crystal. Despite—or perhaps because of—the dispersion anomaly caused by the Reststrahlen band in GaSe, a region of strong lattice resonances that separates the MIR and THz regions, simultaneous phase-matched EOS was successfully achieved for both regions—through SFG for MIR detection:

$$\omega_{\mathrm{SFG}}^{\mathrm{e-wave}} = \omega_{\mathrm{gate}}^{\mathrm{o-wave}} + \omega_{\mathrm{MIR}}^{\mathrm{o-wave}},$$

and DFG for THz detection,

$$\omega_{\mathrm{DFG}}^{\mathrm{e-wave}} = \omega_{\mathrm{gate}}^{\mathrm{o-wave}} - \omega_{\mathrm{MIR}}^{\mathrm{o-wave}},$$

within the same phase-matching configuration of the crystal. Here, "o-wave" and "e-wave" refer to the ordinary and extraordinary waves in GaSe, respectively. As a result, high-resolution MIR and THz spectra of ammonia (NH_3, 2-mbar pressure) were retrieved in a single measurement [81]. The characteristic THz and MIR

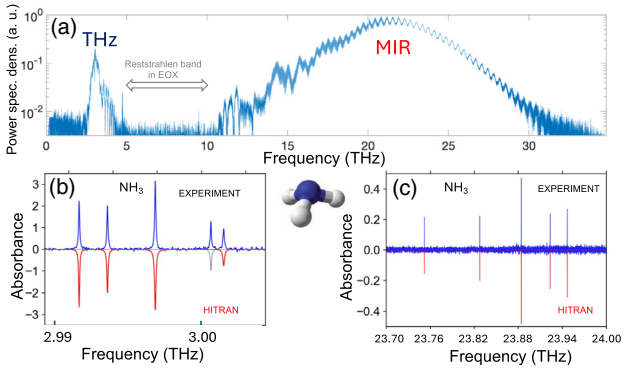

Fig. 7. (a) Combined MIR–THz frequency comb spectrum detected by EOS via SFG (MIR range) and DFG (THz range) processes. (b),(c) High-resolution spectra of the NH_3 molecule measured simultaneously (b) in the MIR and (c) in the THz range. The downward peaks are a simulation based on the HITRAN database.

absorption peaks of NH_3 are displayed in Fig. 7(b) and Fig. 7(c), correspondingly. The spectra were acquired by interleaving 11 spectra with gradually shifted frequency combs, thus providing an average data point spacing of $80/11 = 7.3$ MHz, and excellent agreement was observed between the measured and simulated peaks based on the HITRAN database [82].

Overall, the DCS–EOS method enables high-resolution spectroscopy over an extremely broad frequency range while achieving a superior signal-to-noise ratio, surpassing the best cryogenically cooled photon detectors. This capability enables the generation of high-precision spectroscopic data for molecular databases and fundamental studies. The DCS–EOS method also facilitated the rapid acquisition of extensive datasets, capturing hundreds of thousands of comb-mode-resolved spectral points at speeds reaching video rates [78]. Furthermore, it opens new avenues for real-time, non-invasive medical diagnostics by detecting volatile biomarkers in human breath [83].

4. TIME-DOMAIN SENSING OF THE QUANTUM VACUUM

Going beyond the traditional measurement of average electric field amplitudes by EOS in classical spectroscopies, this section introduces direct detection of the fluctuations of the zero-point vacuum electric field at multi-THz frequencies.

A. Theoretical Description

1. Macroscopic Description

In Section 2.C we saw that the total signal measured in the EOS corresponds to the operator $\hat{S} = \hat{S}_{\mathrm{eo}} + \hat{S}_{\mathrm{sn}}$, with the electro-optic $\hat{S}_{\mathrm{eo}}$ and shot-noise $\hat{S}_{\mathrm{sn}}$ contribution. In case when no classical test wave is present, the expectation values of both contributions vanish. In order to characterize quantum fields, it is necessary to extract statistical information beyond just the expectation value of the signal. Such information is contained already in the second statistical moment, i.e., in the signal variance $\mathrm{Var}\hat{S} = \langle \hat{S}^2 \rangle - \langle \hat{S} \rangle^2$. For propagating purely quantum fields without coherent amplitudes, it reduces to $\mathrm{Var}\hat{S} = \langle \hat{S}^2 \rangle$. By calculating this quantity, we have to consider second-order effects in the interaction, so that relying just on Eqs. (2) and (3) might seem insufficient.

In contrast to the first-order term $\hat{S}_{\mathrm{eo}}$, the second-order correction to the total signal $\hat{S}^{(2)}$ possesses correlations with $\hat{S}_{\mathrm{sn}}$, so that in the variance, it would appear in the same order as $\langle \hat{S}_{\mathrm{eo}}^2 \rangle$. This correction corresponds to the so-called cascaded processes [84–86], illustrated in Fig. 8 in terms of the microscopic density matrix evolution by the corresponding ladder diagrams, together with the $\langle \hat{S}_{\mathrm{eo}}^2 \rangle$ contribution. However, when signals obtained from the photodetectors are integrated over all involved photon frequencies without spectral filtering, and there is no asymmetry in efficiency between the SFG and DFG processes, the contribution of $\langle \hat{S}^{(2)} \hat{S}_{\mathrm{sn}} + \hat{S}_{\mathrm{sn}} \hat{S}^{(2)} \rangle$ vanishes. This happens due to the symmetry of the factor $\int_0^\infty \mathrm{d}\omega |E_G(\omega + \Omega)|^2$ (taking into account the limited bandwidth of E_G) upon the transformation $\Omega \to -\Omega$, as this factor enters the resulting integral over Ω with the opposite signs for Ω and $-\Omega$. Based on that, we can view this fact as a consequence of the indistinguishability between the involved SFG and DFG processes, which is destroyed in the case of frequency cuts upon detection, as exemplified in Fig. 2(b). Upon full integration, we have then

$$\langle \hat{S}^2 \rangle = \langle \hat{S}_{\mathrm{eo}}^2 \rangle + \langle \hat{S}_{\mathrm{sn}}^2 \rangle, \tag{4}$$

where $\langle \hat{S}_{\mathrm{sn}}^2 \rangle = N$ corresponds to the standard shot-noise contribution from the gate pulse. In general, $\langle \hat{S}_{\mathrm{eo}}^2 \rangle$ depends on the particular quantum state of $\hat{E}_{\mathrm{T}}$. For the most fundamental case, when it represents the vacuum, a calculation based on Eq. (3) and accounting for spatial confinement in the transverse direction set by the gate pulse, leads to [32]

$$\langle \hat{S}_{\mathrm{eo}}^2 \rangle = N^2 \left(n^3 \frac{l \omega_G}{c} r_{41} \right)^2 \frac{\hbar \int_0^\infty \mathrm{d}\Omega \Omega (n/n_\Omega) |R(\Omega)|^2}{4\pi^2 \epsilon_0 c n w_0^2}. \tag{5}$$

Here, w_0 is the beam waist radius of the gate pulse, n_Ω and n are the refractive index values at frequencies Ω and ω_{G}, whereas the gating function $R(\Omega)$ and other quantities are introduced in Eqs. (2) and (3). Since the vacuum state is homogeneous in time, the result does not depend on the time delay t_{D}. The first two factors on the right-hand side of Eq. (5) can be viewed as the sampling efficiency. The remaining factor represents, in fact, the variance of the sampled vacuum field and can be written as

$$(\Delta E_{\mathrm{vac}})^2 = \frac{\hbar}{\epsilon_0 \Delta x \Delta y \Delta z \Delta t}. \tag{6}$$

Here, the transverse area $\Delta x \Delta y$ is determined by the beam waist area of the probe, proportional to w_0^2. The ratio of c to the integral containing the gating function $R(\Omega)$, as it appears in Eq. (5), determines the longitudinal cross-sectional area. It corresponds to the effective spatial length Δz times the temporal duration Δt of the gate pulse, with some adjustment due to the phase-matching conditions and the refractive index n_Ω inside the EOX [32].

It was possible to extend the theoretical description above using Green's tensor-based macroscopic quantum electrodynamics [87,88]. This allowed to take care of the absorption effects, and to consider dispersion effects more carefully as well as to go beyond the paraxial approximation exploited in the derivation of Eq. (5). The corresponding corrections might be important to consider or to mitigate [89] when comparing with experimental results.

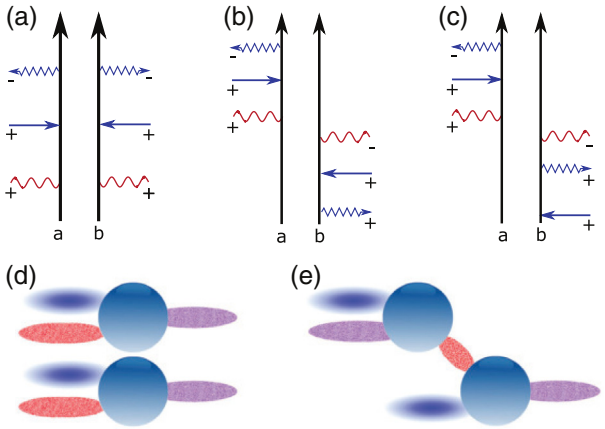

Fig. 8. (a)–(c) Diagrams representing all possible off-resonant microscopic interactions in the parametric processes contributing to the signal of the electric-field vacuum fluctuations, $\mathrm{Var}\hat{S} = \langle \hat{S}^2 \rangle$, on top of the shot-noise contribution N. Each diagram depicts interactions between the electric field modes and the density matrix of the matter system. The vertical arrows indicate the time evolution corresponding to spatial sites a and b from the past (bottom) to the present (top), respectively. The red wavy lines denote an interaction with both positive (annihilation) and negative (creation) frequency parts of $\hat{E}_{\mathrm{T}}$. The blue zigzag arrows pointing to the left (right) represent interactions with the creation (annihilation) part of $\hat{E}_{\mathrm{DFG+SFG}}$, whereas the straight blue arrows pointing to the left (right) denote interactions with the negative (positive) frequency part of the classical component of the coherent field E_{G}. The $\pm$ signs next to the horizontal arrows indicate the type of superoperator interaction for the corresponding field mode, whereas $-$ (+) means the commutator (anticommutator) type. The diagram in (a) describes $\langle \hat{S}_{\mathrm{eo}}^2 \rangle$, containing the information from the existing test wave field $\hat{E}_T$, even if it is just the vacuum here, whereas in the diagrams (b) and (c), photons of the lower frequency field are generated and then absorbed during the corresponding cascading processes. (d),(e) An additional visualization of these processes in terms of the involved atomic sites. The gate pulse (blue) and the lower frequency vacuum (red) interact with the matter at two spatial sites (spheres) to generate a new contribution in the frequency range of the gate pulse (violet). The two processes happen independently of each other in (d), corresponding to the diagram in (a). Alternatively, gate pulse and vacuum modes in the same frequency range interact with the matter at one site to generate a lower frequency field. The generated lower frequency component together with the gate pulse then interacts with the matter at the second site to generate a contribution to the field at the frequencies of the gate pulse. This covers the cascading contributions in (b) and (c). The figure is adapted from Ref. [84].

2. *Microscopic Description*

The considerations in the foregoing sub-section and Section 2 were based on a macroscopic description of the non-linear process in the EOX by means of a macroscopic non-linear susceptibility. It is insightful, however, to analyze these processes and the resulting signals at a microscopic level of the light–matter interaction. A convenient way to implement that is within the superoperator formalism [90], which also allows for insightful diagrammatic visualization of the interaction steps and the corresponding calculations leading to the final signals. Within this formalism, the signal $\mathrm{Var}\hat{S} = \langle \hat{S}^2 \rangle$ can be calculated for the incoming vacuum, starting from a microscopic Hamiltonian for light–matter interaction in the dipole approximation [84]. It can be shown that in the off-resonant case, allowing only for parametric non-linear-optical processes, which is typical for the regimes where EOS is used,

this formalism is actually equivalent to an effective Hamiltonian or wave-equation-based description as above, but with so-called cascaded processes included.

The corresponding diagrams describing the contributions to the signal within the rotating wave approximation (RWA) are depicted in Fig. 8. All depicted contributions can be captured by the effective Hamiltonian description with classical susceptibilities. The contribution in (a) and (d) contains the information on the incoming test wave field, whereas for the contributions corresponding to (b), (c), and (e), the lower frequency field serves only as a mediator at an intermediate step of a cascading process, so that there can be no dependence on the incoming test wave. In terms of the characterization of that test wave, the cascading contributions should be avoided or subtracted in an appropriate way. For testing the field fluctuations, the former option can be realized when the photons are collected from the whole spectral range of the gate pulse. In case of any frequency filtering, required, e.g., to get access to the conjugate field quadrature in the time domain [91,92] for pulsed states of quantum light [93,94], cascading contributions arise and significantly contaminate the measurement. A possibility to mitigate these effects is described in Ref. [95].

B. Quantum Fluctuations on the Sub-Cycle Time-Scale, Experiment

In Section 4.A, we touched on the central role that the measurement apparatus plays in quantum metrology, in that the variance of the sampled quantum field is inversely proportional to the space–time volume occupied by the said measurement device. Making the connection to the discussion on the role of the gating pulse as a temporal local oscillator (Section 2.C) helps us realize that the gating pulse of the EOS serves as a generalized detector that travels at a c/n speed, thereby setting a reference frame where the measurement of quantum fluctuations is averaged over the detector's localized space–time geometry. This concept is schematized in Fig. 9(a), where we visualize a snapshot of the quantum field ground state E_{vac} as positive and negative (red and blue) fluctuations distributed in the transverse (x, y) direction, for fixed z and t coordinates. The detection volume is then set by a space–time region $\Delta x\Delta y\Delta z\Delta t$ taken up by the femtosecond gate pulse, whose duration (τ_{G}) and spatial extent (w_0) control the magnitude of the quantum signal, with a larger gate leading to the averaging out of the quantum noise. It should be emphasized that the detection of a bare vacuum field does not require a scan of a variable temporal delay, as the ground state's temporal mode is automatically synchronized with the gate pulse. More formally, an appearance of a characteristic feature size in Fig. 9(a) is ascribed to the averaging of field fluctuations with high values of the four-wavevector $(\omega, \boldsymbol{k})$, in other words, introducing a filter with a $(|\Delta\boldsymbol{k}_{\mathrm{f}}|, \Delta\omega_{\mathrm{f}})$ passband. As an example, let us illustrate this process along the longitudinal direction. The non-linear signal depends on the response function of the detector $R(\omega)$ (see Section 2.B), which is a product of the phase-matching function and the power spectral density of the intensity of the gate pulse $I_{\mathrm{G}}(\omega)$. For the fixed experimental conditions, namely ω_{T} and ω_{G}, it is the choice of the non-linear crystal which sets the phase-matching bandwidth $\Delta\omega_{\mathrm{PM}}$ centered at ω_{T}, thus carving out a frequency response window $\Delta\omega_{\mathrm{f}}$ of the detection process. On the other hand, $I_{\mathrm{G}}(\omega)$, integrated over the $\Delta\omega_{\mathrm{PM}}$, controls the signal strength, which can be adjusted by changing the duration of the gate pulse. This understanding informs the experimental procedure for isolating the quantum contribution $\langle\hat{S}^2_{\mathrm{eo}}\rangle$ from the total signal variance $\langle\hat{S}^2\rangle$ as per Eq. (4):

I. Measure with the maximally focused space-time extent of the gate, obtaining $\langle\hat{S}^2_{\mathrm{F}} = \hat{S}^2_{\mathrm{eo}} + \hat{S}^2_{\mathrm{sn}}\rangle$;
II. Measure with defocused space-time volume of the gate, i.e., $\langle I_{\mathrm{G}}(\omega_{\mathrm{T}})\rangle \to 0$: $\langle\hat{S}^2_{\mathrm{eo}}\rangle \to 0$ and $\langle\hat{S}^2_{\mathrm{D}}\rangle = \langle\hat{S}^2_{\mathrm{sn}}\rangle$;

The ratio of the two measurements yields a normalized total variance: $\langle\hat{S}^2_{\mathrm{F}}\rangle/\langle\hat{S}^2_{\mathrm{D}}\rangle = 1 + \langle\hat{S}^2_{\mathrm{eo}}\rangle/\langle\hat{S}^2_{\mathrm{sn}}\rangle$, a measure of excess polarization noise of the gate beam, arising from its coupling to the incoming quantum field E_{vac}.

Let us now follow the estimate of excess noise based on the first experimental measurement of a quantum vacuum field using EOS [31,32]. First, we rewrite Eq. (6) [23]:

$$\Delta E_{\mathrm{vac}} = \sqrt{\frac{\hbar\omega_{\mathrm{T}}\Delta\omega_{\mathrm{PM}}}{\epsilon_0(2\pi)^2 w_0^2 c n}}, \tag{7}$$

where we introduced effective transverse and longitudinal cross-sections of the gate beam, given by $\Delta x\Delta y = \pi w_0^2$ and $\Delta z\Delta t = c\pi^2/(n\omega_{\mathrm{T}}\Delta\omega_{\mathrm{PM}})$, respectively. Using Eq. (5), we define the noise-equivalent electric field of EOS:

$$\Delta E_{\mathrm{sn}} = \frac{c}{\omega_{\mathrm{G}} l r_{41} n^3 R(\omega_{\mathrm{T}})\sqrt{N}}, \tag{8}$$

where N is the mean photon number in the assumed Poisson photon number distribution of the gate beam. Finally, using

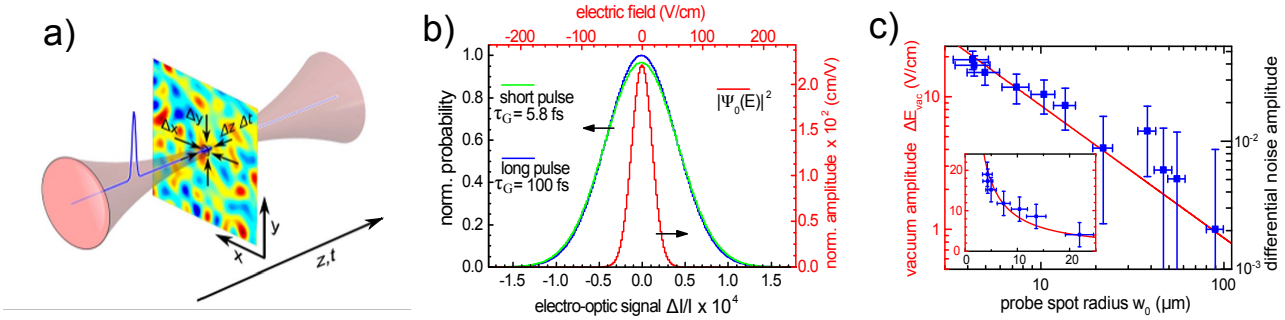

Fig. 9. (a) Schematic of the experiment: a spatio-temporally focused probe beam propagates along the z direction through the EOX, together with a vacuum field under study (amplitude fluctuations are represented by blue–red spatial configuration). (b) Distributions of EOS measurement outcomes for a temporally focused ($\tau_G = 5.8$ fs, green) and defocused ($\tau_G = 100$ fs, blue) probe pulse. Red distribution corresponds to the distilled vacuum contribution. (c) Scaling of the measured magnitude of the vacuum field with the changing probe size (blue squares) compared with the theoretical prediction (red line). This is adapted from Ref. [31].

experimentally determined values for a 5.8 fs gate pulse ($\omega_G/2\pi = 255$ THz; $w_0 = 4.25$ μm; $N = 5 \times 10^8$); $AgGaS_2$ EOX ($n = 2.4$; $l = 30$ μm; $r_{41} = 7.58$ pm/V) and the response function ($\omega_T/2\pi = 67.5$ THz; $\omega_{PM}/2\pi = 66$ THz; $R(\omega_T) = 0.41$), we arrive at $\Delta E_{vac} = 20.2$ V/cm and $\Delta E_{sn} = 65$ V/cm, corresponding to a 4.7% increase in the noise due to the coupling of the gate pulse to the MIR quantum vacuum field.

Figures 9(b) and 9(c) show the results of the experiments [31] that compare total measurement noise for the case of the smallest space–time volume of the gate (maximal coupling to the vacuum field, step I) with the cases when the EO detector space–time volume is enlarged either in longitudinal (panel b) or transverse (panel c) direction (both cases providing an estimation of the shot noise contribution, step II). In Fig. 9(b), each of the two noise measurements is summarized in a normalized probability distribution, containing 10^8 readouts of the relative differential photocurrent $p(\Delta I/I)$. The temporally focused 5.8 fs gate pulse (green) is compared to the 100 fs defocused case (blue), obtained by chirping the former via a small insertion of additional glass material in a Brewster-prism compressor. This ensures that N (and correspondingly the spectral content) of the temporally focused and defocused gate remains unchanged. The observed 4% increase in the root mean square (RMS) amplitude of the detected field fluctuations $(\langle \hat{S}_F \rangle^2 / \langle \hat{S}_D^2 \rangle)^{1/2}$ when focused case is compared to the defocused one is a direct measure of the quantum contribution of the MIR electromagnetic ground state, which is also in good agreement with the theoretical estimate of 4.7% [23]. The whole quantum noise distribution can be extracted from the measurement set by performing a deconvolution procedure, after the realization that the focused case (green) is obtained by a convolution of the shot noise distribution (blue) with the one arising from the quantum contribution (shown in red). Formally, the red distribution corresponds to one quadrature of the measured quantum vacuum field in the space–time volume defined by the focused gate pulse. Since the overall distribution of the quantum ground state is rotationally symmetric in the space spanned by the two (orthogonal) quadratures, the obtained red distribution represents a measurement of a projection of the square of the wavefunction of the quantum field ground state $|\Psi_{vac}|^2$ onto a quadrature within a mode, defined by the gating pulse. In Fig. 9(c), the extracted contribution of the vacuum amplitude ΔE_{vac} is plotted for a set of measurements (blue squares) where the gating pulse is progressively defocused in the transverse direction. Agreement with the theoretical description is evident when the dataset is compared with the direct plot of $\Delta E_{vac}(w_0)$ in Eq. (7) (red line), i.e., assuming no fitting parameters. Both transverse and longitudinal dilation of the space–time volume yield equivalent measurements, substantiated by the quantitative theoretical predictions, which leads us to conclude that the EOS technique can provide a direct measure of the quantum vacuum field distribution, localized over the space–time geometry of the detector. This feat is enabled by the subcycle nature of the temporal gating procedure of electro-optic sampling, where the condition of $\tau_G < 2\pi/\omega_T$ provides an efficient interaction with the virtual particle creation and annihilation events of the vacuum sea, occurring on the characteristic timescale set by $2\pi/\omega_T$ [85]. Furthermore, excitations of the quantum field can, in principle, also be measured with the same technique, where an external perturbation pulse would excite the quantum field under study (e.g., a pump pulse generating a squeezed vacuum [94,95]), and the gating pulse would probe the evolution of the quantum noise contribution as a function of the delay between the two pulses. An upgrade of the EOS technique toward full quantum state tomography would then be desirable.

5. CORRELATION MEASUREMENTS USING ELECTRO-OPTIC SAMPLING

The EOS-based time-resolved technique for characterizing quantum fields, as discussed in Section 4, can also be extended to measure their correlations. One can legitimately trace back the origin of correlation measurements in quantum optics to the ground breaking experiments by Hanbury Brown and Twiss [96] who searched to unravel correlations in the light's intensity $I(\vec{r}, t)$ rather than in its amplitude $E(\vec{r}, t)$ at two space–time points $(\vec{r}, t)$ and $(\vec{r} + \delta\vec{r}, t + \tau)$, by measuring the quantity $g^{(2)}(\vec{r}, \vec{r}', \tau) = \langle I(\vec{r}, t) I(\vec{r} + \delta\vec{r}, t + \tau) \rangle$. These remarkable experiments have shown that photons from a thermal source tend to bunch together. Although nowadays such quantity is typically measured by analyzing the correlation of the signal from two detectors that are directly sensitive to light's intensity, remarkably, the initial proposal and demonstration of the effect was performed in the context of radio astronomy using electric field detectors, necessitating to infer the optical intensity by squaring the voltage output of the radio receiver antenna. This historic example underpins the possibility to measure correlations through electric field-sensitive techniques, such as EOS. The understanding of the implication of these experiments for non-classical sources required Glauber's theory of coherences.

Conceptually, translating the Hanbury Brown and Twiss (HBT) experiment to MIR and terahertz frequencies can simply be achieved by implementing the EOS technique with two gate pulses (Fig. 10). While the quantum state under study $|\psi\rangle$ is not read out directly via receiver antennas, as was the case in the original HBT experiment, the electro-optic sampling technique achieves a conceptually equivalent outcome by reading out the polarization state of the two gate pulses. This is because upconverting the time-domain quantum state to the NIR or visible domain via non-linear frequency mixing maintains the entire information about the electric field with sub-cycle spatio-temporal resolution, as is discussed in Sections 2.B and 2.C. Apart from this additional experimental necessity, the analogy remains valid in that the goal is to be able to unravel the quantum statistical properties of MIR and THz radiation through field measurements.

In the prototypical correlation experiment based on EOS, the quantum test wave is sent into a non-linear crystal together with the two gate pulses. As visible from Fig. 10, the much larger frequency of the gate pulses allows for their much tighter focusing, achieving a much smaller cross-section compared to the one of the quantum states under study. By acting on the displacement and angle of the mirror M in Fig. 10, this allows to shift the two gate pulses in time or space and hence investigates space–time dependent correlations in the fields. By aligning the two gate beams at a slight angle of each other, they can be analyzed separately and on a single-shot basis even when $\delta\vec{r} = 0$. This allows to directly reconstruct the electric field correlations $g^{(1)}(\vec{r}, \delta\vec{r}, \tau) = \langle \hat{E}(\vec{r}, t) \hat{E}(\vec{r} + \delta\vec{r}, t + \tau) \rangle \sim \langle \{ \hat{S}(\vec{r}, t), \hat{S}(\vec{r} + \delta\vec{r}, t + \tau) \} \rangle$ through multiplication of the read-outs of the electro-optic signal $\hat{S} = \hat{S}_{eo} + \hat{S}_{sn}$ from the two gate pulses and subsequent averaging of their product, acquired at a rate equal to the

repetition rate of the laser. Squaring the fields before averaging would then allow to also study the intensity correlation $g^{(2)}(\vec{r}, \delta\vec{r}, \tau) = \langle \hat{E}^2(\vec{r}, t)\hat{E}^2(\vec{r}+\delta\vec{r}, t+\tau)\rangle$.

Such a two-beam correlation measurement will lead to non-zero averages for any field, even those that are not phase-locked to the probing laser. Measuring correlations instead of the electric field, however, comes with the challenge of longer integration times. The single-shot signal-to-noise measurement for a field measurement is equal to $\mathrm{SNR}_{\mathrm{single-shot},E-\mathrm{field}} = \frac{E_T(\vec{r},t)}{\mathrm{NEF}}$, with $E_T(\vec{r}, t)$ the field of the quantum state and NEF, the noise equivalent field for a single laser pulse measurement, cf. Eq. (8). Even in the limit of vanishingly small technical noise and thus shot-noise-limited detection, typical values are currently around $\mathrm{SNR}_{\mathrm{single-shot},E-\mathrm{field}} \sim 10^{-3}$ for quantum states in the terahertz frequency range. Consequently, the signal-to-noise ratio for an electric field correlation measurement is very low, about $\mathrm{SNR}_{\mathrm{single-shot},g(1)} = (\frac{E_T(\vec{r},t)}{\mathrm{NEF}})^2 \sim 10^{-6}$, that can be easily confirmed by analyzing the definition of $g^{(1)}(\vec{r}, \delta\vec{r}, \tau)$.

Given these challenging signal-to-noise conditions, the key aspect of the correlation technique is that the contribution of the shot noise of the gate pulses $\langle \hat{S}_{\mathrm{sn}}(\vec{r}, t)\hat{S}_{\mathrm{sn}}(\vec{r}+\delta\vec{r}, t+\tau)\rangle$ to the correlation signal is averaged toward zero by making sure that the intensity fluctuations of the two gate pulses are uncorrelated. This is achieved by creating the two gate pulses by splitting a single gate pulse into two at the lossless beam splitter shown in Fig. 10, which admixed uncorrelated vacuum through its open port. A derivation can be found in quantum optics textbooks such as the one by Loudon [97].

The journey toward measuring the correlations in free-running quantum fields started with the measurement of classical fields. Worthwhile mentioning are initial measurements of classical, coherent states from a quantum cascade laser as a first step of transitioning from the more established EOS of phase-locked THz pulses toward single-mode, free-running laser fields from other sources. The initial scheme still required locking of the terahertz semiconductor laser to the femtosecond oscillator sampling it to ensure phase stability [98,99]. The development of two-probe sampling schemes, however, opened EOS to all sorts of emission, irrespective of their phase properties, including free-running classical, coherent states, and hence $|\psi\rangle = |\alpha\rangle_\Omega$. Indeed, in Refs. [100,101], the authors used the technique to measure the $g^{(1)}$ and $g^{(2)}$ and the transition from the spontaneous to the coherent emission of a THz quantum cascade laser [Fig. 10(b)].

In these initial experiments, the benefit of electro-optic correlation measurement schemes was not immediately visible as it could be (somewhat mistakenly) regarded as being entirely equivalent to the measurement in a Fourier transform infrared spectrometer (FTIR). The latter interferes with two copies of a field that pass through a Michelson interferometer to retrieve the quantity $\langle E(t)E(t+\tau)\rangle$, with τ being dictated by the difference in the two arms. The striking difference between the two techniques becomes evident when recalling that this interference is measured using an intensity detector, limiting its applicability to optical modes that are characterized by a non-zero number of photons.

In contrast, the electro-optic correlation technique is, at its core, a technique that measures fields instead of intensities, allowing to study correlations even in quantum states that are characterized by zero photons, opening the path for vacuum field fluctuations and hence $|\psi\rangle = |0\rangle_\Omega$. In experiments performed in the THz range, correlations prevailing even at cryogenic temperatures where thermal occupation was vanishingly small [Fig. 10(c)], could then be attributed to vacuum field fluctuations [102]. More recently, the ability of this technique to reveal correlations on sub-cycle spatio-temporal scales turned out to provide answers to fundamental questions in quantum electrodynamics that were inaccessible before [103]. Feynman himself predicted the existence of correlations of vacuum field fluctuations outside the light cone—meaning for space–time points that are causally disconnected ($\delta\vec{r} > c\tau/n_\Omega$) and cannot become correlated through the exchange of a real photon. The challenge is that such correlations become vanishingly small at the boundary of the light cone ($\delta\vec{r} = c\tau/n_\Omega$). The capability of the electro-optic correlation technique to measure very small fluctuations was then instrumental to demonstrating Feynman's predictions experimentally [104] [Fig. 10(d)].

An analogous scheme has been exploited to investigate thermal spin fluctuations around a phase transition in a weak ferromagnet [105,106]. The short correlation lengths of collective excitations in the condensed phase, such as magnons, favor focusing under high numerical aperture in such experiments. Therefore, the two probe pulses were set to slightly different wavelengths and separated by a dichroic beam splitter before polarization analysis. Time-domain correlation data, as illustrated in Fig. 10(e), provide direct information about magnon dynamics and discrete switching phenomena of the magnetization without requiring excitation of the system.

6. ADVANCED CONCEPTS AND FUTURE DIRECTIONS

After describing the fundamentals of EOS with selected applications in linear spectroscopy and quantum optics, this section completes our survey with a roadmap of progress that we expect for the next future. Some of these steps have already been studied thoroughly by theoretical work, while experimental implementations remain to be demonstrated.

A. Improving Sensitivity and Spectral Coverage of EOS Measurements

The key performance metric of the EOS method is detection sensitivity, which is currently constrained by the shot noise of the gate laser pulses. To push the sensitivity closer to the ultimate limit—the shot noise of the *test wave* for the measurement of classical fields—one strategy is to enhance the upconversion efficiency of the test wave (ideally close to 100%) in the EOX, which can be achieved by employing strong gate pulses. A high conversion efficiency of up to several percent in the SFG configuration was achieved in Refs. [29,107]. The authors demonstrated that, despite the depletion of test-wave photons, detection linearity can still be maintained by applying the methods described in their work. Additional measures for sensitivity improvement include using balanced detectors with the highest possible saturation power to reduce the shot noise associated with the detection of the gate laser pulses, properly designed spectral filtering (see Section 2), lock-in modulation [31], or rapid scanning of the test wave delay, particularly for measurements that do not require high spectral resolution [29].

The phase-matched DFG EOS configuration can be used similarly to SFG (see e.g. [78]), with the main difference that the test wave is parametrically amplified upon co-propagating with the

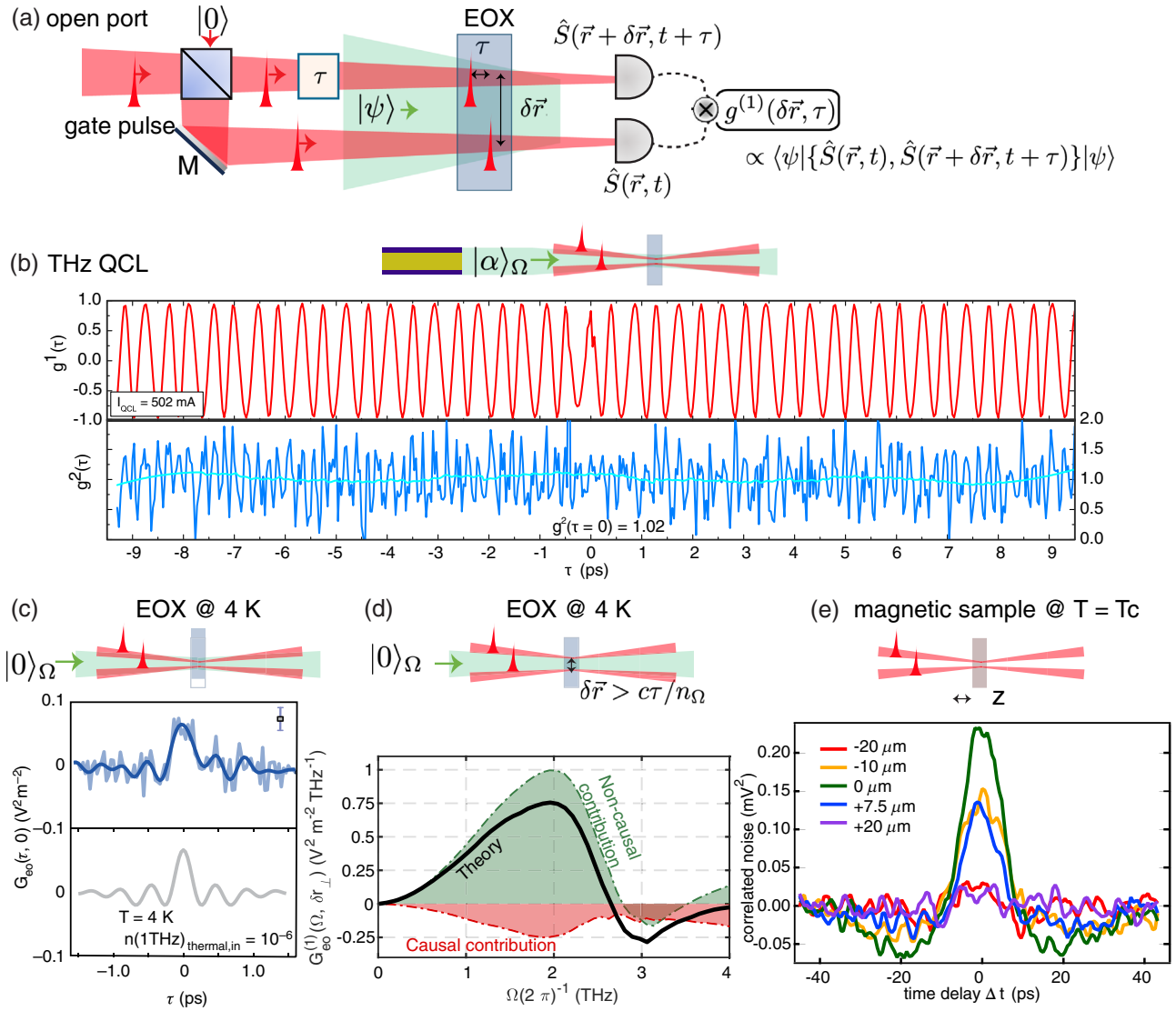

Fig. 10. (a) Two-probe correlation scheme. A single gate pulse is split into two at a 50:50 beam splitter. After one of the two is delayed by a time τ, the two sample an arbitrary terahertz quantum state $|\psi\rangle$ at two space–time points $(\vec{r}, t)$ and $(\vec{r}+\delta\vec{r}, t+\tau)$. $\delta\vec{r}$ is controlled by acting on the mirror M after the beam splitter. The two gate pulses perform two measurements on the electric field of the quantum state, and the first-order coherence function is computed through multiplication of the readouts of the electro-optic signal $\hat{S} = \hat{S}_{eo} + \hat{S}_{sn}$, followed by averaging. This yields $G_{eo}(\tau, \delta\vec{r}) = \langle\psi|\hat{E}(\vec{r}, t)\hat{E}(\vec{r}+\delta\vec{r}, t+\tau)|\psi\rangle$. (b) Measurements of first- and second-order correlation functions $g^{(1)}(\tau)$ and $g^{(2)}(\tau)$ on light emitted by a classical source, a THz quantum cascade laser (QCL) [100]. The coherent, single-mode character of the emission is revealed by $g^{(1)}(\tau)$ that oscillates with a frequency equal to the oscillation frequency of the laser. The Poissonian statistics of the laser emission are confirmed since the average value of $g^{(2)}(\tau = 0) = 1$(light blue line). (c) Electric field correlation in vacuum field fluctuations, measured by placing the non-linear crystal (EOX) shown in panel (a) into a cryogenic environment at $T = 4$ K, and choosing $|\psi\rangle = |0\rangle_\Omega$, denoting the vacuum field at terahertz frequencies [102]. Experimentally, this is achieved by removing any source from the environment. A non-zero value of $G_{eo}(\tau, 0)$ reveals the coherence time of vacuum field fluctuations. (d) Measurements of correlations on vacuum fields with spatially displaced beams where $\delta\vec{r} > c\tau/n_\Omega$ allows to study correlations existing outside the light cone [104]. Their frequency content has causal and non-causal contributions. (e) The technique in panel (a) has also been adapted to measure correlations in the magnetization of ferroelectric materials around a phase transition happening at critical temperature T_c [105]. This was achieved by exploiting the magneto-optical effect instead of the electro-optic effect. The various curves reveal how noise correlations in the magnetization depend on various positions of the sample along z, which influences the sampled space–time volume. This is adapted from Refs. [100,102].

gate pulse through the EOX [Fig. 2(a), right panel]. This amplification effect [30] might also hold the potential for increasing the sensitivity of EOS.

In terms of spectral coverage, Zimin *et al*. recently advanced the capabilities of EOS to allow for broadband field-resolved measurements in the visible and potentially ultraviolet (UV) ranges [15]. Their approach utilized SFG to mix the gate and test waves, with the resulting wave interfering with the third harmonic of the gate pulse, which acted as a local oscillator. Notably, in this demonstration, the center frequency of the gate pulse was lower than that of the test waveform.

B. Beyond Quantum Vacuum Measurements

Having achieved direct detection and correlation analysis of the electromagnetic quantum vacuum at MIR and THz frequencies

[31,102], it is, of course, tempting to go for subcycle quantum analysis of more complex quantum states of the light field. Studying coherent waves would not represent an attractive goal, as their electric-field variance corresponds exactly to the one of the vacuum, rendering them the most "classical-like" states one can think of. In contrast, squeezed vacuum states should provide a variance of the electric field that periodically falls below and rises above the vacuum level in a characteristic fashion. The first variant of such an experiment, together with a simplified theory explanation, was presented in 2017 [93]. Further, a consistent theory of the generation and detection of sybcycle dynamics of the quantum noise for the ultrabroadband pulsed squeezed vacuum was developed in Ref. [94]. Related to the presence of significant coherent field amplitudes in those measurements, strong parasitic noise deviations in the EOS arose that contaminated the fluctuation patterns based on a combination of the effects described in Refs. [92,108]. One way to move forward with time-domain analysis of MIR squeezed light would be to exploit an intense source of phase-stable MIR transients [109] and to generate a squeezed vacuum by spontaneous parametric fluorescence that may be isolated from the coherent pump by polarization filtering. The procedures may be generalized to produce non-Gaussian ultrabroadband pulsed states of light, e.g., by utilizing appropriate postelection schemes [95].

C. Quantum State Tomography

To characterize ultrabroadband quantum states of light, such as discussed in Section 6.A, it is generally insufficient to have access only to the variance of the corresponding electric field operator in the time domain or to its second-order correlations. A complete local characterization of these states leads to the idea of time-domain tomography with subcycle resolution. In principle, a tomographic reconstruction can be based upon the projection of the pulsed quantum light to a set of localized temporal modes constituting a complete orthogonal basis for its decomposition [110,111]. However, this procedure is based on an explicit or implicit assumption that these modes are known, e.g., by the virtue of the generation method. A question arises what to do if this assumption is lifted? How to obtain a sufficiently complete local picture of quantum light, such as a single photon, at the most fundamental of its characteristic timescales, namely the oscillation cycle of its mode or its inverse frequency? The answer leads to the concept of subcycle tomography of quantum light [95,112,113].

In order to advance in that direction, it is necessary first to address the issue of how to introduce and measure a conjugate field quadrature in the time domain, mentioned in Section 4. It was shown in Ref. [91] that in a version of the EOS setup, with a different waveplate in the ellipsometry part and appropriate frequency filtering for the detected gate pulse frequencies, it is possible to create a situation where the DFG- and SFG-related contributions are combined with the opposite phases. This enables local access to the Hilbert transform of the test wave, i.e., the field shifted by $\frac{\pi}{2}$ in its carrier-envelope phase (CEP) with respect to the original waveform [91,92,94,114]. Theory predicts that an adjusted scheme allows for the sampling of the signal determined by the field of the test wave shifted by any value in its CEP [89,94,95].

Functions reconstructed from tomography protocols represent joint quasi-probability distributions of the sampled instantaneous electric field and its conjugated generalized quadrature. A novel feature emerging in the context of the topic of this review is access to these distributions with subcycle temporal resolution, based on appropriate definitions and measurement protocols. As known from quantum optics, there are different types of quasi-probability distributions [34], providing in the considered case information on the ultrafast evolution of the characteristic quantum-optical and quantum-informational features of the studied pulsed states of light, such as photon content, squeezing, metrological power [115], and eventually negativity [34]. It has been proposed that having access to the quantum statistics of both time-domain quadratures, it is possible to sample the time-resolved positive Q-distribution [34] by measuring their joint quantum statistics [112,113] at each time delay t_D, whereby only Gaussian states have been addressed theoretically in this way. Understanding the space-time geometry of the two quadratures yields routes for multiplexing and mode-matching operations on the gating function for the efficient detection of each of the quadratures [113]. Alternatively, it is possible to gather quantum statistics for a set of CEP-rotated quadratures, whereby reconstructing a sufficient number of statistical moments and cross-moments of both quadratures to obtain a time-resolved Wigner function for any time point [95]. In order to reconstruct non-Gaussian states or if we are agnostic to the fact if the state under study is Gaussian or not, higher statistical moments of the quadratures are required, whereas their accurate acquisition within the EOS framework might demand advanced methods, e.g., as elucidated in Section 6.E.

D. Measurement Back-Action

The description of the EOS is of a perturbative nature in terms of the induced changes in the polarization properties of the gating pulse and the resulting EOS signal. For certain applications, it might be tempting to increase the strength of this pulse, e.g., in order to improve the signal-to-noise ratio in the characterization of weak classical and quantum fields. By doing so, first, the perturbative non-linear-optical description may break down due to the initiation of higher-order nonlinearities beyond $\chi^{(2)}$ [86,116]. Second, the EOS process can start to influence the analyzed test wave itself due to various $\chi^{(2)}$ cascading effects [84–86]. Such a measurement back-action effect in the EOS was thoroughly investigated in Ref. [86] for the case of quantum vacuum fluctuations, both in the single-beam and two-beam configurations. It was found that back-action starts to significantly distort the test wave in the EOX, and, therefore, the resulting EOS signal, when the variance of the EOS contribution $\langle \hat{S}^2_{\mathrm{eo}} \rangle \propto N^2$ to the total variance $\langle \hat{S}^2 \rangle$ becomes comparable to the shot-noise contribution $\langle \hat{S}^2_{\mathrm{sn}} \rangle = N$, as it scales faster with the increase of the gate pulse strength reflected by its total photon number N. Using the notion of the shot-noise equivalent field of EOS ΔE_{sn}, introduced in Section 4.B, this condition means that the electric-field amplitude of the vacuum fluctuations ΔE_{vac} is not anymore negligible with respect to ΔE_{sn}. In other words, quantum EOS measurement is only reliable in the weak measurement regime, without a significant impact of back-action. The development of new EOS-based schemes to mitigate back-action is an important future research direction toward more precise and efficient characterization of quantum fields in the time domain.

E. Quantum-Enhanced EOS with Non-Classical Gates

As alluded to in Section 6.B, the non-linear process of parametric downconversion provides an attractive mechanism for generating ultrafast bright quantum light [117], especially once combined

with phase-locked driving [109]. In the context of EOS, it is also interesting to consider promoting the gate pulse to the quantum state, especially in the form of a bright two-mode squeezed vacuum, where quantum correlations between the distinguishable signal and idler beams can be exploited for enhanced detection [118]. In particular, it was predicted that the EO signal and the sensitivity to higher-order statistical moments could be increased when using the signal twin as a gate pulse and applying an engineered post-selection protocol on the measurement outcomes in the square-law detector of the idler twin. Quantum test signals with distinctly non-Gaussian statistics (e.g., Schrödinger cat, N00N, etc. states) possess characteristics expressed in statistical moments beyond their variance. As was shown, quantum gate pulses with distinct non-Gaussian statistics provide better sensitivity to probing such states than the EOS gates with Poissonian distribution [118]. Very recent advances have reported quantum-enhanced EOS detection using twin beams [119]. One of the important requirements is to keep the quantum gate in a single spatiotemporal mode, which was recently demonstrated through the generation of near-IR 10 fs twin beam pulses with a mean photon number in excess of 10^8 [120] and robust quantum correlations in the carrier envelope phase [121], thus paving the way to future exploration of quantum-enhanced EOS.

F. Intra-Cavity Experiments

All measurements discussed in this review were performed in bulk non-linear crystals, enabling studies on broadband quantum states of light. This is in strong contrast to cavity quantum electrodynamics experiments, which typically concentrate on one cavity mode.

Ongoing efforts to bridge the two realms concentrate on developing means to add cavities to electro-optic sampling experiments as a way to shape the density of states and spatial distribution of terahertz quantum fields. Integrated terahertz photonics may offer highly sub-wavelength confinement toward vacuum fields exceeding 10 V/m and ways to sample these fields at specific space–time points by exploiting the platform's ability to route optical waveguides toward any location. Initial studies demonstrate intra-cavity on-chip terahertz detection [122–124] and generation [125,126] of phase-locked terahertz pulses in hybrid silicon-organic or thin film lithium niobate. While these measurements would potentially benefit from increased field sensitivity and, consequently, a larger $\mathrm{SNR}_{\mathrm{single-shot},E-\mathrm{field}} = \frac{E_T(\vec{r},t)}{\mathrm{NEF}}$, and $\mathrm{SNR}_{\mathrm{single-shot},g(1)} = (\frac{E_T(\vec{r},t)}{\mathrm{NEF}})^2$, an experimental demonstration of characterizing incoherent sources, e.g., through electro-optic correlations is still outstanding.

The ease of integration with other material platforms, such as superconductors [127] or semiconductors [128], may then enable long cavity lifetimes or studies of non-adiabatic switching of such cavities under irradiation with femtosecond pulses. Other benefits arise from the platform's ability to engineer the dispersion characteristics (group velocity and group velocity dispersion) of gate pulses on-chip and thereby prevent the otherwise probable walk-off of the SFG and DFG signals discussed in Section 2.B.

G. Relativistic Aspects

The ability to sample quantum fields and their correlations in localized regions of space–time opens intriguing avenues for inquiry into quantum statistics and relativity. On the one hand, the measurement of correlations in two space–time regions outside each other's light cone [103] calls for the question of whether such correlation could be used for entanglement harvesting. A recent proposal shows that such an experiment is conceptually feasible and predicts protocols for constructing states with correlations that would violate a Bell inequality, assuming some improvements in the efficiency of the EOS detection [129]. In another instance, fascinating insight unfolds when one considers the operation of quantum-optical squeezing directly in the time domain. As shown theoretically [94], temporal refractive index modulation caused by a strong classical pump beam propagating through a non-linear crystal can be viewed, in a dressed medium picture, as a difference between the lab time and the conformal time inside the crystal. Remarkably, this leads to a modification of statistics of a co-propagating quantum field, dynamically causing its noise redistribution (e.g., squeezed quantum vacuum). There is thus a thought-provoking interplay of quantum statistics and geometry of space–time, perhaps motivating experimental exploration of such analogies.

7. CONCLUSION

Electro-optic sampling (EOS) has proven to be a transformative technique, enabling the full characterization of electric-field waveforms in both amplitude and phase. Meanwhile, its influence extends beyond its original scope, sparking advancements across diverse fields such as ultrafast phenomena in complex systems, high-precision and high-dynamic-range molecular spectroscopy in both condensed and gas phases, and time-domain quantum electrodynamics. Looking ahead, the future of EOS research promises exciting developments. These include expanding the technique to field-resolved measurements in the ultraviolet (UV) and potentially extreme ultraviolet (XUV) ranges, exploring the tomography of quantum fields in space–time, and leveraging quantum-enhanced EOS with non-classical gates. Additionally, performing intra-cavity experiments, developing on-chip terahertz-wave detection, and investigating quantum statistics and relativistic effects are poised to push the boundaries of this versatile tool even further.

Funding. Air Force Office of Scientific Research (FA9550-23-1-0126); U.S. Department of Energy (BR #KA2601020); Deutsche Forschungsgemeinschaft (Project ID 425217212, SFB 1432, Project-ID 390713860); Ministry of Science and ICT, South Korea (2020R1A2C1008500); Natural Sciences and Engineering Research Council of Canada; Canada Research Chairs; Fonds de recherche du Québec -Nature et technologies; Institut Transdisciplinaire d'Information Quantique; European Union's Horizon Europe Research and Innovation Programme (101070700, project MIRAQLS); State Research Center OPTIMAS; European Research Council (101088303).

Acknowledgment. K. L. V. acknowledges funding from the AFSOR and the U.S. Department of Energy. A. L. and A. S. M. acknowledge funding from the DFG. A.S.M. was supported by the NRF grant funded by the MSIT. D. V. S. acknowledges received funding by the NSERC via the CRC; the FRQNT via INTRIQ, and the European Union's Horizon Europe Research and Innovation Programme. I.P. Acknowledges funding from the DFG, the State Research Center OPTIMAS, and the European Research Council. I.C.B.C. acknowledges funding from the Swiss National Science Foundation and the European Union.

Disclosures. The authors declare no conflicts of interest.

Data availability. Experimental data are available upon reasonable request.

REFERENCES

1. F. Pockels, *Lehrbuch der Kristalloptik* (Teubner, 1906).

2. P. Sibson, C. Erven, M. Godfrey, *et al.*, "Chip-based quantum key distribution," Nat. Commun. **8**, 13984 (2017).
3. M. Kourogi, K. Nakagawa, and M. Ohtsu, "Wide-span optical frequency comb generator for accurate optical frequency difference measurement," IEEE J. Quant. Electron. **29**, 2693–2701 (1993).
4. L. A. Valdmanis, G. A. Mourou, and C. W. Gabel, "Subpicosecond electrical sampling," IEEE J. Quant. Electron. **19**, 664–667 (1983).
5. D. H. Auston, K. P. Cheung, J. A. Valdmanis, *et al.*, "Cherenkov radiation from femtosecond optical pulses in electro-optic media," Phys. Rev. Lett. **53**, 1555 (1984).
6. Q. Wu and X. C. Zhang, "Free-space electro-optic sampling of terahertz beams," Appl. Phys. Lett. **67**, 3523–3525 (1995).
7. A. Nahata, A. S. Weling, and T. F. Heinz, "A wideband coherent terahertz spectroscopy system using optical rectification and electro-optic sampling," Appl. Phys. Lett. **69**, 2321–2323 (1996).
8. G. Gallot and D. Grischkowsky, "Electro-optic detection of terahertz radiation," J. Opt. Soc. Am. B **16**, 1204–1212 (1999).
9. Q. Wu and X. C. Zhang, "Free-space electro-optics sampling of MIR pulses," Appl. Phys. Lett. **71**, 1285–1286 (1997).
10. A. Leitenstorfer, S. Hunsche, J. Shah, *et al.*, "Detectors and sources for ultrabroadband electro-optic sampling: experiment and theory," Appl. Phys. Lett. **74**, 1516 (1999).
11. A. Sell, A. Leitenstorfer, and R. Huber, "Phase-locked generation and field-resolved detection of widely tunable terahertz pulses with amplitudes exceeding 100 MV/cm," Opt. Lett. **33**, 2767–2769 (2008).
12. C. Kübler, R. Huber, S. Tübel, *et al.*, "Ultrabroadband detection of multi-THz field transients with GaSe electro-optic sensors: approaching the near infrared," Appl. Phys. Lett. **85**, 3360 (2004).
13. A. Sell, R. Scheu, A. Leitenstorfer, *et al.*, "Field-resolved detection of phase-locked infrared transients from a compact Er:fiber system tunable between 55 and 107 THz," Appl. Phys. Lett. **93**, 251107 (2008).
14. S. Keiber, S. Sederberg, A. Schwarz, *et al.*, "Electro-optic sampling of near-infrared waveforms," Nat. Photonics **10**, 159 (2016).
15. A. Zimin, V. S. Yakovlev, and N. Karpowicz, "Ultra-broadband all-optical sampling of optical waveforms," Sci. Adv. **8**, eade1029 (2022).
16. D. Grischkowsky, S. Keiding, M. van Exter, *et al.*, "Far-infrared time-domain spectroscopy with terahertz beams of dielectrics and semiconductors," J. Opt. Soc. Am. B **7**, 2006–2015 (1990).
17. B. Ferguson and X. C. Zhang, "Materials for terahertz science and technology," Nat. Mater. **1**, 26–33 (2002).
18. P. U. Jepsen, D. G. Cooke, and M. Koch, "Terahertz spectroscopy and imaging–modern techniques and applications," Laser Photonics Rev. **5**, 124–166 (2011).
19. J. Neu and C. A. Schmuttenmaer, "Tutorial: an introduction to terahertz time domain spectroscopy (THz-TDS)," J. Appl. Phys. **124**, 231101 (2018).
20. R. McElroy and K. Wynne, "Ultrafast dipole solvation measured in the far infrared," Phys. Rev. Lett. **79**, 3078–3081 (1997).
21. M. C. Beard, G. M. Turner, and C. A. Schmuttenmaer, "Transient photoconductivity in GaAs as measured by time-resolved terahertz spectroscopy," Phys. Rev. B **62**, 15764–15777 (2000).
22. R. Huber, F. Tauser, A. Brodschelm, *et al.*, "How many-particle interactions develop after ultrafast excitation of an electron–hole plasma," Nature **414**, 286–289 (2001).
23. C. Riek, D. V. Seletskiy, and A. Leitenstorfer, "Femtosecond measurements of electric fields: from classical amplitudes to quantum fluctuations," Eur. J. Phys. **38**, 024003 (2017).
24. W. Cho, J. Shin, and K. T. Kim, "Reconstruction algorithm for tunneling ionization with a perturbation for the time-domain observation of an electric-field," Sci. Rep. **11**, 13014 (2021).
25. J. Dai, X. Xie, and X. C. Zhang, "Detection of broadband terahertz waves with a laser-induced plasma in gases," Phys. Rev. Lett. **97**, 103903 (2006).
26. C. Y. Li, D. V. Seletskiy, Z. Yang, *et al.*, "Broadband field-resolved terahertz detection via laser induced air plasma with controlled optical bias," Opt. Express **23**, 11436–11443 (2015).
27. K. Liu, J. Xu, and X. C. Zhang, "GaSe crystals for broadband terahertz wave detection," Appl. Phys. Lett. **85**, 863–865 (2004).
28. M. Porer, J. M. Ménard, and R. Huber, "Shot noise reduced terahertz detection via spectrally postfiltered electro-optic sampling," Opt. Lett. **39**, 2435–2438 (2014).
29. I. Pupeza, M. Huber, M. Trubetskov, *et al.*, "Field-resolved infrared spectroscopy of biological systems," Nature **577**, 52–59 (2020).
30. C. Hofer, "Detection efficiency and bandwidth optimized electro-optic sampling of MIR waves," Dissertation (LMU München, Fakultät für Physik, 2021).
31. C. Riek, D. V. Seletskiy, A. S. Moskalenko, *et al.*, "Direct sampling of electric-field vacuum fluctuations," Science **350**, 420–423 (2015).
32. A. S. Moskalenko, C. Riek, D. V. Seletskiy, *et al.*, "Paraxial theory of direct electro-optic sampling of the quantum vacuum," Phys. Rev. Lett. **115**, 263601 (2015).
33. E. Ridente, M. Mamaikin, N. Altwaijry, *et al.*, "Electro-optic characterization of synthesized infrared-visible light fields," Nat. Commun. **13**, 1111 (2022); Supplementary information.
34. W. Vogel and D. Welsch, *Quantum Optics* (Wiley, 2006).
35. T. Gabbrielli, F. Cappelli, N. Bruno, *et al.*, "MIR homodyne balanced detector for quantum light characterization," Opt. Express **29**, 14536–14547 (2021).
36. R. Trebino, *Frequency-Resolved Optical Gating: The Measurement of Ultrashort Laser Pulses* (Springer, 2000).
37. L. A. Wu, H. J. Kimble, J. L. Hall, *et al.*, "Generation of squeezed states by parametric down conversion," Phys. Rev. Lett. **57**, 2520–2523 (1986).
38. P. R. Griffiths and J. A. De Haseth, *Fourier Transform Infrared Spectrometry*, 2nd ed., Vol. **171** of Chemical Analysis (Wiley-Interscience, 2007).
39. W. Demtröder, *Molecular Physics* (Wiley-VCH Verlag GmbH, 2005).
40. M. J. Baker, J. Trevisan, P. Bassan, *et al.*, "Using Fourier transform IR spectroscopy to analyze biological materials," Nat. Protoc. **9**, 1771–1791 (2014).
41. M. Huber, K. V. Kepesidis, L. Voronina, *et al.*, "Stability of person-specific blood-based infrared molecular fingerprints opens up prospects for health monitoring," Nat. Commun. **12**, 1511 (2021).
42. K. Yeh, I. Sharma, K. Falahkheirkhah, *et al.*, "Infrared spectroscopic laser scanning confocal microscopy for whole-slide chemical imaging," Nat. Commun. **14**, 5215 (2023).
43. H. Timmers, A. Kowligy, A. Lind, *et al.*, "Molecular fingerprinting with bright, broadband infrared frequency combs," Optica **5**, 727–733 (2018).
44. A. V. Muraviev, V. O. Smolski, Z. E. Loparo, *et al.*, "Massively parallel sensing of trace molecules and their isotopologues with broadband subharmonic MIR frequency combs," Nat. Photonics **12**, 209–214 (2018).
45. T. P. Butler, D. Gerz, C. Hofer, *et al.*, "Watt-scale 50-MHz source of single-cycle waveform-stable pulses in the molecular fingerprint region," Opt. Lett. **44**, 1730–1733 (2019).
46. C. Gaida, M. Gebhardt, T. Heuermann, *et al.*, "Watt-scale super-octave MIR intrapulse difference frequency generation," Light Sci. Appl. **7**, 94 (2018).
47. A. Catanese, J. Rutledge, M. C. Silfies, *et al.*, "MIR frequency comb with 67 W average power based on difference frequency generation," Opt. Lett. **45**, 1248–1251 (2020).
48. U. Elu, L. Maidment, L. Vamos, *et al.*, "Seven-octave high-brightness and carrier-envelope-phase-stable light source," Nat. Photonics **15**, 277–280 (2021).
49. S. Vasilyev, I. S. Moskalev, V. O. Smolski, *et al.*, "Super-octave longwave MIR coherent transients produced by optical rectification of few-cycle 2.5-μm pulses," Optica **6**, 111–114 (2019).
50. P. Täschler, M. Bertrand, B. Schneider, *et al.*, "Femtosecond pulses from a MIR quantum cascade laser," Nat. Photonics **15**, 919–924 (2021).
51. Q. Ru, T. Kawamori, P. G. Schunemann, *et al.*, "Two-octave-wide (3–12 μm) subharmonic produced in a minimally dispersive optical parametric oscillator cavity," Opt. Lett. **46**, 709–712 (2021).
52. P. Steinleitner, N. Nagl, M. Kowalczyk, *et al.*, "Single-cycle infrared waveform control," Nat. Photonics **16**, 512–518 (2022).
53. S. A. Hussain, C. Hofer, M. Högner, *et al.*, "Sub-attosecond-precision optical-waveform stability measurements using electro-optic sampling," Sci. Rep. **14**, 20869 (2024).
54. W. Schweinberger, L. Vamos, J. Xu, *et al.*, "Interferometric delay tracking for low-noise Mach-Zehnder-type scanning measurements," Opt. Express **27**, 4789–4798 (2019).

55. M. Huber, M. Trubetskov, W. Schweinberger, *et al.*, "Standardized electric-field-resolved molecular fingerprinting," Anal. Chem. **96**, 13110 (2024).
56. M. T. Peschel, M. Högner, T. Buberl, *et al.*, "Sub-optical-cycle light-matter energy transfer in molecular vibrational spectroscopy," Nat. Commun. **13**, 5897 (2022).
57. M. Huber, M. Trubetskov, S. A. Hussain, *et al.*, "Optimum sample thickness for trace analyte detection with field-resolved infrared spectroscopy," Anal. Chem. **92**, 7508–7514 (2020).
58. C. Hofer, D. Bausch, L. Fürst, *et al.*, "Linear field-resolved spectroscopy approaching ultimate detection sensitivity," Opt. Express **33**, 1–17 (2025).
59. O. Schubert, M. Eisele, V. Crozatier, *et al.*, "Rapid-scan acousto-optical delay line with 34 kHz scan rate and 15 as precision," Opt. Lett. **38**, 2907–2910 (2013).
60. A. Weigel, P. Jacob, D. Gröters, *et al.*, "Ultra-rapid electro-optic sampling of octave-spanning MIR waveforms," Opt. Express **29**, 20747–20764 (2021).
61. A. Weigel, P. Jacob, W. Schweinberger, *et al.*, "Dual-oscillator infrared electro-optic sampling with attosecond precision," Optica **11**, 726–735 (2024).
62. S. M. Teo, B. K. Ofori-Okai, C. A. Werley, *et al.*, "Invited article: single-shot THz detection techniques optimized for multidimensional THz spectroscopy," Rev. Sci. Instrum. **86**, 051301 (2015).
63. D. Gerz, M. Huber, H. Mirkes, *et al.*, "High-speed field-resolved infrared fingerprinting of particles in flow," in *Conference on Lasers and Electro-Optics/Europe (CLEO/Europe) and European Quantum Electronics Conference (EQEC)*, Technical Digest Series (Optica Publishing Group, 2023), paper cl_2_1.
64. F. Blanchard, A. Doi, T. Tanaka, *et al.*, "Real-time terahertz near-field microscope," Opt. Express **19**, 8277–8284 (2011).
65. F. Blanchard and K. Tanaka, "Improving time and space resolution in electro-optic sampling for near-field terahertz imaging," Opt. Lett. **41**, 4645–4648 (2016).
66. Y. Zhao, L. Zhang, G. Duan, *et al.*, "Single-pixel terahertz imaging via compressed sensing," Proc. SPIE **8195**, 81950Q (2011).
67. R. I. Stantchev, D. B. Phillips, P. Hobson, *et al.*, "Compressed sensing with near-field THz radiation," Optica **4**, 989–992 (2017).
68. M. Mamaikin, Y. L. Li, E. Ridente, *et al.*, "Electric-field-resolved near-infrared microscopy," Optica **9**, 616–622 (2022).
69. F. Keilmann, C. Gohle, and R. Holzwarth, "Time-domain MIR frequency-comb spectrometer," Opt. Lett. **29**, 1542–1544 (2004).
70. F. N. Picqué and T. W. Hänsch, "Frequency comb spectroscopy," Nat. Photonics **13**, 146–157 (2019).
71. I. Coddington, N. Newbury, and W. Swann, "Dual-comb spectroscopy," Optica **3**, 414–426 (2016).
72. I. O. Kara, L. Maidment, T. Gardiner, *et al.*, "Dual-comb spectroscopy in the spectral fingerprint region using OPGaP optical parametric oscillators," Opt. Express **25**, 32713–32721 (2017).
73. M. Yan, P. L. Luo, K. Iwakuni, *et al.*, "MIR dual-comb spectroscopy with electro-optic modulators," Light Sci. Appl. **6**, e17076 (2017).
74. I. G. Ycas, F. R. Giorgetta, E. Baumann, *et al.*, "High-coherence MIR dual comb spectroscopy spanning 2.6 to 5.2 μm," Nat. Photonics **12**, 202–208 (2018).
75. S. Vasilyev, A. Muraviev, D. Konnov, *et al.*, "Longwave infrared (6.6–11.4 μm) dual-comb spectroscopy with 240,000 comb-mode-resolved data points at video rate," Opt. Lett. **48**, 2273–2276 (2023).
76. Y. D. Hsieh, Y. Iyonaga, Y. Sakaguchi, *et al.*, "Spectrally interleaved, comb-mode-resolved spectroscopy using swept dual terahertz combs," Sci. Rep. **4**, 3816 (2014).
77. A. S. Kowligy, H. Timmers, A. J. Lind, *et al.*, "Infrared electric field sampled frequency comb spectroscopy," Sci. Adv. **5**, eaaw8794 (2019).
78. D. Konnov, A. Muraviev, S. Vasilyev, *et al.*, "High-resolution frequency-comb spectroscopy with electro-optic sampling and instantaneous octave-wide coverage across MIR to THz at a video rate," APL Photonics **8**, 110801 (2023).
79. S. Vasilyev, I. Moskalev, V. Smolski, *et al.*, "Kerr-lens mode-locked Cr:ZnS oscillator reaches the spectral span of an optical octave," Opt. Express **29**, 2458–2465 (2021).
80. P. Sulzer, M. Högner, A. K. Raab, *et al.*, "Cavity-enhanced field-resolved spectroscopy," Nat. Photonics **16**, 692–697 (2022).
81. D. Konnov, A. Muraviev, and K. L. Vodopyanov, "Simultaneous high-resolution dual-comb spectroscopy of rovibrational and rotational bands of ammonia," in *17th International HITRAN Conference*, Cambridge, Massachusetts, 2024, p. 3.
82. I. E. Gordon, L. S. Rothman, R. J. Hargreaves, *et al.*, "The HITRAN2020 molecular spectroscopic database," J. Quant. Spectrosc. Radiat. Transfer **277**, 107949 (2022).
83. A. Wang and P. Sahay, "Breath analysis using laser spectroscopic techniques: breath biomarkers, spectral fingerprints, and detection limits," Sensors **9**, 8230 (2009).
84. M. Kizmann, A. S. Moskalenko, A. Leitenstorfer, *et al.*, "Quantum susceptibilities in time-domain sampling of electric field fluctuations," Laser Photonics Rev. **16**, 2100423 (2022).
85. S. Onoe, T. L. M. Guedes, A. S. Moskalenko, *et al.*, "Realizing a rapidly switched Unruh-DeWitt detector through electro-optic sampling of the electromagnetic vacuum," Phys. Rev. D **105**, 056023 (2022).
86. T. L. M. Guedes, I. Vakulchyk, D. V. Seletskiy, *et al.*, "Back action in quantum electro-optic sampling of electromagnetic vacuum fluctuations," Phys. Rev. Res. **5**, 013151 (2023).
87. F. Lindel, R. Bennett, and S. Y. Buhmann, "Theory of polaritonic quantum-vacuum detection," Phys. Rev. A **102**, 041701 (2020).
88. F. Lindel, R. Bennett, and S. Y. Buhmann, "Macroscopic quantum electrodynamics approach to nonlinear optics and application to polaritonic quantum-vacuum detection," Phys. Rev. A **103**, 033705 (2021).
89. M. Kizmann, "Theory of ultrashort quantum states and their detection through electro-optic sampling," Ph.D. thesis (University of Konstanz , Konstanz, Germany, 2022). http://nbn-resolving.de/urn:nbn:de:bsz:352-2-ef3oevwtn7n26.
90. S. Mukamel, *Principles of Nonlinear Optical Spectroscopy* (Oxford University, 1995).
91. P. Sulzer, K. Oguchi, J. Huster, *et al.*, "Determination of the electric field and its Hilbert transform in femtosecond electro-optic sampling," Phys. Rev. A **101**, 033821 (2020).
92. S. Virally and B. Reulet, "Unidimensional time-domain quantum optics," Phys. Rev. A **100**, 023833 (2019).
93. A. Riek, P. Sulzer, M. Seeger, *et al.*, "Subcycle quantum electrodynamics," Nature **541**, 376–379 (2017).
94. M. Kizmann, T. L. M. Guedes, D. V. Seletskiy, *et al.*, "Subcycle squeezing of light from a time flow perspective," Nat. Phys. **15**, 960–966 (2019).
95. G. Yang, M. Kizmann, A. Leitenstorfer, *et al.*, "Subcycle tomography of quantum light," arXiv (2023).
96. R. Hanbury Brown and R. Q. Twiss, "Correlation between photons in two coherent beams of light," Nature **177**, 27–29 (1956).
97. R. Loudon, *The Quantum Theory of Light* (Oxford University, 2000).
98. A. Oustinov, N. Jukam, R. Rungsawang, *et al.*, "Phase seeding of a terahertz quantum cascade laser," Nat. Commun. **1**, 69 (2010).
99. S. Barbieri, M. Ravaro, P. Gellie, *et al.*, "Coherent sampling of active mode-locked terahertz quantum cascade lasers and frequency synthesis," Nat. Photonics **5**, 306–313 (2011).
100. I. C. Benea-Chelmus, C. Bonzon, C. Maissen, *et al.*, "Subcycle measurement of intensity correlations in the terahertz frequency range," Phys. Rev. A **93**, 043812 (2016).
101. I.-C. Benea-Chelmus, M. Rösch, G. Scalari, *et al.*, "Intensity autocorrelation measurements of frequency combs in the terahertz range," Phys. Rev. A **96**, 033821 (2017).
102. I. C. Benea-Chelmus, F. F. Settembrini, G. Scalari, *et al.*, "Electric field correlation measurements on the electromagnetic vacuum state," Nature **568**, 202–206 (2019).
103. F. F. Settembrini, F. Lindel, A. M. Herter, *et al.*, "Detection of quantum-vacuum field correlations outside the light cone," Nat. Commun. **13**, 3383 (2022).
104. A. Lindel, A. M. Herter, J. Faist, *et al.*, "Probing vacuum field fluctuations and source radiation separately in space and time," Phys. Rev. Res. **5**, 043207 (2023).
105. M. A. Weiss, A. Herbst, J. Schlegel, *et al.*, "Discovery of ultrafast spontaneous spin switching in an antiferromagnet by femtosecond noise correlation spectroscopy," Nat. Commun. **14**, 7651 (2023).
106. M. A. Weiss, F. S. Herbst, S. Eggert, *et al.*, "Subharmonic lock-in detection and its optimization for femtosecond noise correlation spectroscopy," Rev. Sci. Instrum. **95**, 083005 (2024).
107. C. Hofer, D. Gerz, M. Gebhardt, *et al.*, "Electro-optic sampling with percent-level detection efficiency," in *Conference on Lasers and*

Electro-Optics Europe (CLEO/Europe-EQEC), Munich, Germany, 2021, p. 1.
108. P. Sulzer, C. Beckh, A. Liehl, *et al.*, "Passive elimination of correlated amplitude fluctuations in ultrabroadband supercontinua from highly nonlinear fibers by three-wave mixing," Opt. Lett. **45**, 4714–4717 (2020).
109. H. Kempf, A. Muraviev, F. Breuning, *et al.*, "Direct sampling of femtosecond electric-field waveforms from an optical parametric oscillator," APL Photonics **9**, 036111 (2024).
110. J. Roslund, R. M. De Araujo, S. Jiang, *et al.*, "Wavelength-multiplexed quantum networks with ultrafast frequency combs," Nat. Photonics **8**, 109–112 (2014).
111. Y. S. Ra, A. Dufour, M. Walschaers, *et al.*, "Non-Gaussian quantum states of a multimode light field," Nat. Phys. **16**, 144–147 (2020).
112. A. Hubenschmid, T. L. M. Guedes, and G. Burkard, "Optical time-domain quantum state tomography on a subcycle scale," Phys. Rev. X **14**, 041032 (2024).
113. S. Onoe, S. Virally, and D. V. Seletskiy, "Direct measurement of the Husimi-Q function of the electric-field in the time-domain," arXiv (2023).
114. C. Riek, P. Sulzer, M. Seeger, *et al.*, "Simultaneous sampling of electric field quadratures in the time domain," in *Conference on Lasers and Electro-Optics*, OSA Technical Digest (Optical Society of America, 2016), paper SM1L.1.
115. A. Kwon, K. C. Tan, T. Volkoff, *et al.*, "Nonclassicality as a quantifiable resource for quantum metrology," Phys. Rev. Lett. **122**, 040503 (2019).
116. R. W. Boyd, *Nonlinear Optics*, 3rd ed. (Academic, 2008).
117. M. V. Chekhova, G. Leuchs, and M.Żukowski, "Bright squeezed vacuum: entanglement of macroscopic light beams," Opt. Commun. **337**, 27–43 (2015).
118. S. Virally, P. Cusson, and D. V. Seletskiy, "Enhanced electro-optic sampling with quantum probes," Phys. Rev. Lett. **127**, 270504 (2021).
119. D. Adamou, L. Hirsch, T. Shields, *et al.*, "Quantum-enhanced time-domain spectroscopy," Sci. Adv. **11**, eadt2187 (2025).
120. P. Cusson, A. Rasputnyi, F. Tani, *et al.*, "Ultrafast bright squeezed vacuum in nearly single spatio-temporal mode," in *CLEO: Fundamental Science* (2024), paper FTh1M.5.
121. P. Cusson, S. Virally, and D. Seletskiy, "Carrier-envelope phase correlations in few-cycle bright twin beams," in *23rd International Conference on Ultrafast Phenomena* (2024), paper Th-4A.4.
122. I. C. Benea-Chelmus, Y. Salamin, F. F. Settembrini, *et al.*, "Electro-optic interface for ultrasensitive intracavity electric field measurements at microwave and terahertz frequencies," Optica **7**, 498–505 (2020).
123. Y. Salamin, I. C. Benea-Chelmus, Y. Fedoryshyn, *et al.*, "Compact and ultra-efficient broadband plasmonic terahertz field detector," Nat. Commun. **10**, 5550 (2019).
124. A. Tomasino, A. Shams-Ansari, M. Lončar, *et al.*, "500 GHz field-resolved detection in thin-film lithium niobate devices," in *Proceedings of 48th International Conference on Infrared, Millimeter, and Terahertz Waves (IRMMW-THz)* (IEEE, 2023).
125. A. Herter, A. Shams-Ansari, F. F. Settembrini, *et al.*, "Terahertz waveform synthesis in integrated thin-film lithium niobate platform," Nat. Commun. **14**, 11 (2023).
126. Y. Lampert, A. Shams-Ansari, A. Gaier, *et al.*, "Photonics-integrated terahertz transmission lines," arXiv (2024).
127. A. Scalari, C. Maissen, S. Cibella, *et al.*, "High quality factor, fully switchable terahertz superconducting metasurface," Appl. Phys. Lett. **105**, 261104 (2014).
128. M. Halbhuber, J. Mornhinweg, V. Zeller, *et al.*, "Non-adiabatic stripping of a cavity field from electrons in the deep-strong coupling regime," Nat. Photonics **14**, 675–679 (2020).
129. F. Lindel, A. Herter, V. Gebhart, *et al.*, "Entanglement harvesting from electromagnetic quantum fields," Phys. Rev. A **110**, 022414 (2024).